Nanostructure 3D metallic foams as electrocatalysts for electrooxidation and hydrolysis of sodium borohydride

Muhammed Kabir Bello

Thesis to obtain a Master of Science Degree in

Energy Engineering and Management

Supervisors: Dr. Diogo Miguel Franco dos Santos
Dr. Sónia Cristina da Conceição de Matos Eugénio

Examination Committee

Chairperson: Prof. Francisco Manuel da Silva Lemos

Supervisor: Dr. Diogo Miguel Franco dos Santos

Member of the Committee: Prof. César Augusto Correia de Sequeira

October 2017

Acknowledgements.

My immense gratitude goes to my supervisors for their patience, and guidance, all the members of the MemChem research group for their camaraderie, selflessness, and words of encouragement over relished coffee breaks, with a special mention to Ms. Aldona; to whom some of the catalyst owes their sense of purpose. It goes without the need to mention that getting here would have been impossible without my benefactors (EIT's InnoEnergy consortium). To my inexhaustible list of amazing friends, and associates whose contributions to my success might be subliminal, I say thank you. Lastly, I acknowledge the unrelenting support of my family from thousands of miles away, through their prayers and love.

ABSTRACT

The synergistic effect of metallic electrocatalysts based on nickel, copper, cobalt and iron on the electrooxidation as well as hydrolysis of sodium borohydride, were investigated. The nanoporous three-dimensional foam structure of the catalysts was obtained using the dynamic hydrogen bubble template (DHBT), a simple, fast, and low-cost electrodeposition technique. Physicochemical properties were characterized by scanning electron microscopy and energy dispersive X-ray spectroscopy, while electrocatalytic performance was analyzed by cyclic voltammetry at different scan rates. Hydrolysis of sodium borohydride was carried out in an inverted burette setup, and found to be highly imprecise, with better results being obtained using a digital gas meter. Binary foams of nickel and copper ($Ni_{52}Cu_{31}O_{17}$) produced the best performance in terms of number of electrons transferred towards electrooxidation of sodium borohydride, with 4 electrons and a charge transfer coefficient up to 0.81. The maximum oxidation current attributable to borohydride oxidation obtained was 124.7 $mA.cm^{-2}$ for the $Ni_{14}Cu_{26}Fe_{41}O_{18}$ foam, and 13057.59 $mA.g_{cat}^{-1}$ when normalized for mass of catalyst. Co_{100} and $Ni_{62}Co_{24}Fe_{14}$ foams showed no activity towards electrooxidation of the fuel. Co_{100} foam disintegrated for concentrations more alkaline than 1:2 fuels to alkali molar ratio, and had the best yield for hydrogen of 1865.2 mL in 240 minutes, while the ternary $Ni_4Cu_{48}Fe_{30}O_{12}$ produced the most resource efficient performance for hydrolysis with a rate of 157.06 $mL.min^{-1}$ g_{cat}^{-1}.

Contents

1 INTRODUCTION

Promise of clean and efficient power generation characteristic of fuel cell technology - first demonstrated in 1839 by Sir William Grove - is more alive than ever. Since the successful development of fuel cell technology for the American space program in the 1950's, coupled with a space program commercialization policy, we have witnessed an era of substantial development efforts in Japan and the Americas. However, the initial surge of improvement in knowledge and technical issues pertinent to the fuel cell technology was followed by an extended period of stagnation due to the global boom of the fossil based fuel. More recently, in the end of the 20th century global climatic and environmental concerns arising predominantly from extensive use of fossil based fuel, have renewed the enthusiasm in fuel cell technology.

Fuel cells are electrochemical energy devices that convert chemical energy to electricity as long as they are supplied with a fuel and an oxidant. They offer the merits of a heat engine and a battery and eliminate the major drawbacks of both. Fuel cells are fundamentally classified based on the nature of electrolyte employed and of its operating temperatures:

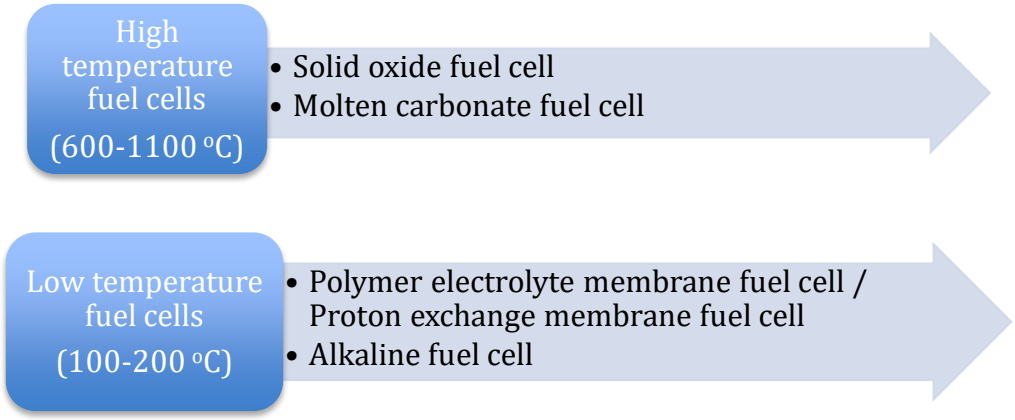

Figure 1.1 Typical fuel cell sub categories.

Polymer electrolyte fuel cells (PEFC) typically operate at temperatures below 80 ^{0}C and are considered the most promising fuel cells for portable and residential applications due to their characteristic high-power density. However, impediments to large-scale deployment of the hydrogen driven technology include: cost competitiveness, engineering design and safety concerns of a hydrogen gas fueled device [1].

The use of safer, spontaneously oxidizing, high specific energy liquid fuels obviously ameliorates the engineering design challenges and improves the economics somewhat. To this effect, methanol in what is referred to as direct methanol fuel cells (DMFC) have found application as fuel, but is subject to a new set of limitations that include: slower kinetics hence lower power for any given cell size, low open circuit potential, inefficient fuel electrooxidation, and methanol crossover between electrodes [2].

The Apollo mission of the 60's, couldn't have been successful without alkaline fuel cells (AFC's). In wake of the successes of PEMFC's, research and developments efforts for alkaline fuel cells were scaled down. However, this kind of fuel cell has numerous advantages. The activation over potential at the cathode is less in comparison to its acidic counterpart, due to the long observed rapid reduction of oxygen in alkaline media. Hence, AFC's have considerably higher cell potential of up to 0.875V than PEMFC's. Also, the low-cost electrolyte and non-precious metal electrode materials reflects on the low system cost of alkaline fuel cells. The simplest type of fuel cells to be manufactured is based on the dissolved fuel principle-characteristic of alkaline fuel cells, which does not favor high power generation. In theory, the dissolved fuel principle is not limited to only alkaline electrolyte fuel cells, but it is very difficult to make a non-precious metal based active catalyst oxidize the fuel in a low temperature acid electrolyte fuel cell [2].

The earlier listed problems associated with using methanol in DMFC's are being overcome by using alternative hydrogen carriers, one of which is sodium borohydride ($NaBH_4$), as the fuel in accordance to the dissolved fuel principle [3].

2 OVERVIEW OF SODIUM BOROHYDRIDE FUEL CELLS

The earliest demonstration of sodium borohydride fuel cells was in the 1960's. Since then, a successful increase of the output of this fuel cell type from 10 to 400W by the Materials and Energy Research Institute (MERIT – indicate city and country) has been achieved. Subsequent reports show the superior performance to its methanol counterpart in capacity value, electrochemical activity, theoretical open circuit voltage (1.64V against 1.21V), fuel efficiency, and power performance at ambient operating temperature. These breakthroughs have intensified research efforts directed towards optimizing its performance [3,4].

Sodium borohydride ($NaBH_4$) has a capacity value of 5.67 $Ah.g^{-1}$ and hydrogen content of 10.6 wt.%. Direct borohydride fuel cell (DBFC) is the generic term for fuel cells in which $NaBH_4$ is directly oxidized, usually employing oxygen or hydrogen peroxide as oxidant, as opposed to the thermodynamically less favored application as a hydrogen carrier, where it is termed as indirect borohydride fuel cell [5].

DBFCs are considered alkaline fuel cells because of their stability in strong, pure and metal-free alkaline medium. In acidic and neutral media, sodium borohydride undergoes hydrolysis significantly. In addition to the aforementioned traits that make this fuel cell type an attractive option for portable applications, BH^-_4 and its oxidation product borate are inert and non-toxic and may be recycled. The alkaline electrolyte, characterized by low corrosion activity, allows for the possibility of using cheap and readily available non-precious metals as anode catalysts. However, this is both a pro and a con as most metals and their compounds, often catalyze the parallel occurring hydrolysis reaction, giving rise to the challenge in the choice of anode electro catalyst for the cell [3]. A schematic of a typical borohydride fuel cell with the important reactions is shown below.

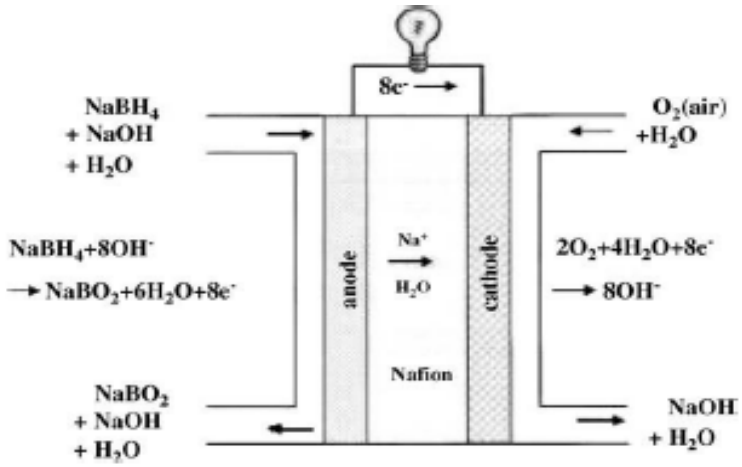

Figure 2.1: Schematic of a DBFC with oxygen as oxidant.

2.1 Reactions occurring in DBFCs.

2.1.1 Anodic Reaction

The oxidation of borohydride in aqueous alkaline medium is proposed to proceed as follows:

$$BH_4^- + 8OH^- \rightarrow BO_2^- + 6H_2O + 8e^- \quad (E^0 = -1.24V \text{ vs. SHE}) \qquad (2.1)$$

Quasi-spontaneous hydrolysis of BH_4^- on a number of electrode materials to generate hydroxy borohydride intermediate and hydrogen according to equations (2.2) and (2.3) have been identified as a challenge with anodic oxidation of borohydride.

$$BH_4^- + H_2O \rightarrow BH_3(OH)^- + H_2 \quad (2.2)$$

$$BH_3(OH)^- + H_2O \rightarrow BO_2^- + 3H_2 \quad (2.3)$$

Due to the presence of atomic hydrogen on DBFC anodes, the anode potential is a mixed potential of equation (2.1) and (2.4) observed to be between -1.24V and -0.828V vs. SHE.

$$H_2 + 2OH^- \rightarrow 2H_2O + 2e^- \quad (E^0 = -0.828V \text{ vs. SHE}) \quad (2.4)$$

Several reaction pathways have been reported in literature in attempts to fully understanding the detailed mechanism of BH^-_4 electro-oxidation. Gyenge et al. [6] concluded that on platinum electrodes BH_4^- undergoes hydrolysis to yield H_2 which then undergoes oxidation between -0.7 to -0.9V vs. Ag/AgCl while direct oxidation of borohydride occurs in the range -0.15 to -0.05V vs. Ag/AgCl. While, on gold electrode the electrooxidation takes place by an electrochemical-chemical-electrochemical (ECE) mechanism involving intermediates.

The description of the competing borohydride hydrolysis is described as:

$$BH_4^- + 2H_2O \rightarrow BO_2^- + 4H_2 \quad (2.5)$$

Due to this reaction, it is experimentally difficult to achieve the 8-electron transfer reaction path leading to complexities in formulating a rationale for optimizing catalyst choice, composition and design.

The actual stoichiometric description of borohydride electro-oxidation is

$$BH_4^- + nOH^- \rightarrow BO_2^- + (n-2)H_2O + (4-\tfrac{n}{2})H_2 + ne^- \quad (2.6)$$

where n refers to the electron exchange value and determines the faradic efficiency of the process.

2.1.2 Cathodic Reaction

Depending on the choice of oxidant, there are two possible cathodic reactions. The reaction with oxygen produces an inferior potential compared to the reaction with peroxide, making this a crucial consideration when choosing oxidant for any intended application.

The cathodic reaction with oxygen is thus:

$$O_2 + 2H_2O + 4e^- \rightarrow 4OH^- \quad (E^0 = 0.40V \text{ vs. SHE}) \quad (2.7)$$

The net cell reaction with oxygen is:

$$2O_2 + NaBH_4 \rightarrow NaBO_2 + 2H_2O \quad (E_0 = 1.64V) \quad (2.8)$$

The cathodic reaction with hydrogen peroxide as oxidant is:

$$H_2O_2 + 2e^- \rightarrow 2OH^- \quad (E^0 = 0.87V \text{ vs. SHE}) \quad (2.9)$$

The net cell reaction with peroxide is:

$$BH_4^- + 4H_2O_2 \rightarrow BO_2^- + 6H_2O \quad (E_0 = 2.11V) \quad (2.10)$$

2.2 Anode Materials

Particles of oxidative dehydrogenation noble metals such as platinum and palladium are a natural choice as electrooxidation electrocatalysts. Supported on nanoporous carbon the results have been outstanding, though accompanied with challenges limited to high cost and alkaline corrosion of the carbon support. Metals are predominantly employed as electro catalysts for low temperature fuel cells. However, the noble metals (silver, gold, platinum, iridium, ruthenium, and palladium) despite their

exemplary performances are economically impractical. In response to this issue, researchers expect that low cost, transition, non-noble metals (nickel, iron, tin, cobalt, molybdenum etc.) with unoccupied *3d* orbitals have the potential to produce a synergistic catalytic effect aimed at enhancing the borohydride oxidation reaction and consequently improving commercial viability of DBFCs.

Some organics such as metal phthalocyanines, and porphyrins have also shown catalytic activity but the nature of the observed activity is yet not fully established. However, based on heat treatment experiments that result in the alteration of the original structure of these organics, conclusive inferences that a 4-nitrogen bond with the central metal atom is the key requirement for their catalytic activity [7].

Metallic materials with a unique ability to reversibly absorb and release copious amounts of hydrogen gas are called hydrogen storage alloys. A variety of these type materials have been studied thus far, but two types; AB_5 (A = a rare earth metal such as La, Ce, Nd, Pr, or Y and B = a non-hydride forming element such as Ni) and AB_2 type (A = Ti, Zr or Hf, and B = a transition metal), stand out in terms of hydrogen storage capability and operational parameters. Since this class of materials can absorb large quantities of hydrogen, they find application as anodic electro catalysts in DBFCs in a bid to suppress hydrogen evolution.

Gold (Au) and silver (Ag) catalysts have been reported to achieve the best electron transfer per mole of the fuel, between 7-8 electrons [4,8]. This high utilization efficiency is due to their low activity towards the hydrolysis of BH_4^-. However, they both exhibit slow kinetics, Au performing slightly better than Ag.

Comparative performance studies of colloidal elements against their alloys on borohydride electrooxidation have been conducted by several researchers, Platinum (Pt) and its alloys (with Au, Ni and Ir) were studied by Gyenge et al [6], while Au and its alloys were investigated by Atwan et al. [9], generally, alloying resulted in reduced particle size. However, further investigation is required to confirm the role of reduced particle size in the observed reaction kinetics improvements as against the mechanistic effects.

On the other hand, nickel (Ni) is popular for its unique affinity for adsorption of hydrogen containing unsaturated organics. As a result, it is receiving the most attention amongst non-noble metals and is a major component in the earlier mentioned hydrogen storage alloys. A downside to Ni electrodes is the formation of stable oxide/hydroxide, which leads to increased polarization in porous electrodes [10].

In the development of bimetallic nanoparticles, copper (Cu), which has an unfavorable susceptibility to oxidation and a tendency to alloy, has been investigated significantly. Since the chemical stability and formation of oxide layers by Ni, is well documented, Santos et al studied the performance of three-dimensional alloys of Ni and Cu in the oxidation of borohydride [11].

2.3 Nernst Equation

Nernst equation is one of the most important equations in electrochemistry. It provides a linkage between the electrode potential of an electrochemical reaction to its standard electrode potential, temperature and concentration of the active chemical species.

$$E = E^0 + \frac{RT}{nF}\ln\frac{C_O}{C_R} \qquad (2.11)$$

Where E is the electrode potential, E^0 is the standard electrode potential, R is the molar gas constant, T is temperature in Kelvin, n is the number of electrons per mole of reactant, F is Faradays constant-representing the amount of charge in one mole of electrons and C_x represent the concentration of the redox species. If a system conforms to the Nernst equation, it is said to be thermodynamically or electrochemically reversible.

2.4 Nano Electrode Synthesis

It is at least sixty years since the transition from macro to micro sized electrodes for use in electroanalytical chemistry begun. The miniaturization of sensing devices drove this transition, leading to the emergence of a variety of micro technologies developed by the semiconductor industry to produce microelectronic chips and microelectromechanical systems (MEMS).

In recent years, advancement in tools have brought about a transition from micro to nanoelectrode dimensions; offering greater opportunities to study electron-transfer kinetics amongst other relevant phenomena. Nanoelectrodes can be defined as electrodes with at least one dimension in the nanometer scale.

There are two broad methods of fabricating such materials, namely: *bottom-up* and *top-down* approaches. The former is generally based on spontaneous formation of materials based on a calculated design usually by a chemist, of the interactions, physical and chemical alike of any involved materials. While the latter is essentially the progressive size reduction of a continuous bulk material to nanoscale, using a variety of lithographic techniques.

2.4.1 Electrodeposition

Italian chemist Luigi Brugnatelli invented electroplating/electrodeposition in 1805. Electrodeposition is a most convenient method to produce porous structures from aqueous solutions. In this process, the rationale is to leverage on the solvent window of the electrolyte, reducing the solvated metal ions without decomposing the solvent. In simpler terms, it is the application of electric current to reduce cations of a desired material from a solution and deposit it as a thin film on a conductive surface of another material (substrate). Figure 2.2 shows the simple electrodeposition of copper from its sulfate solution.

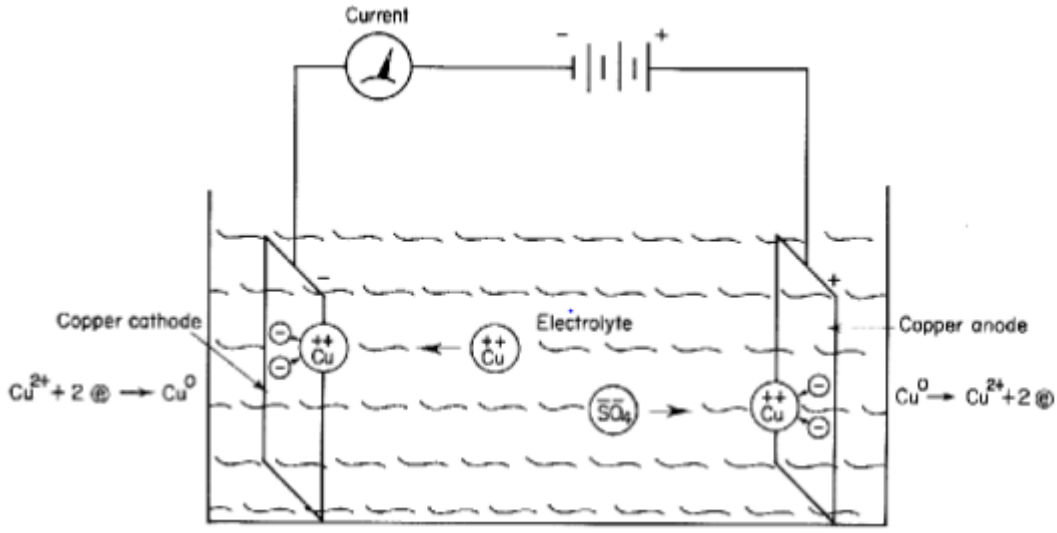

Figure 2.2: Schematic electrolytic deposition of copper from copper sulfate solution [12].

Under the influence of an external electric field, the positive (cations) in the solution are driven to the cathode, were they get reduced and deposited as metallic copper, to maintain the electric neutrality of the solution, copper from the anode dissolves into the solution. If a noble metal such as platinum is employed as the anode instead, the oxidation of water becomes the overall anodic reaction. Since the concentration of copper ions in solution will decrease over time as the concentration of hydrogen ions increases, it will be necessary to introduce more copper sulfate solution and remove hydrogen by neutralization.

The rearrangement of ions in the neighborhood of the electrode surface results in the formation of an electric double layer comprising of the Helmholtz double layer, and a diffuse layer as shown in the figure below. The mechanism of the reaction at the electrode surface occurs as follows:

- Migration: Hydrated metal ions move towards the cathode from the solution under the influence of applied current.
- Electron transfer: The hydrated metal ions then enters the diffuse layer at the cathode surface, where its water molecules are aligned, then proceeds to the Helmholtz double layer where it is deprived of its hydrate envelope.
- Neutralization and adsorption of the dehydrated ion follows.
- The adsorbed atom now migrates to the growth region on the surface.

The thickness of the deposited layer depends on the duration of electroplating, typical thickness is between 0.1 to 30 microns. Figure 2.3 shows the models of electrical double layers; which evolved from Helmholtz model to the more accurate Gouy-Chapman-Stern model.

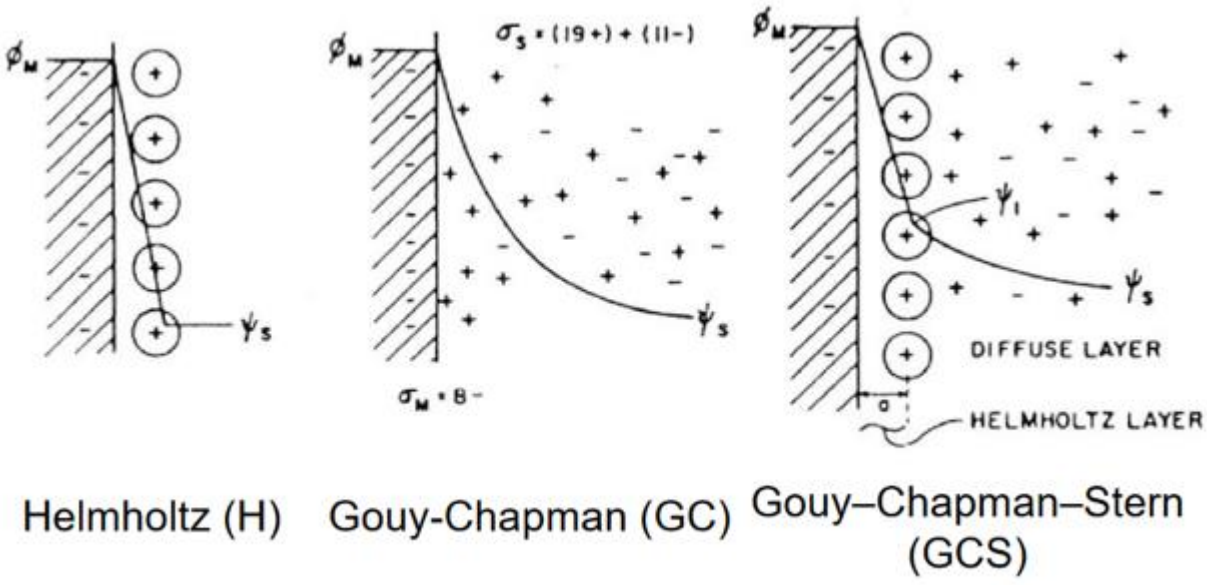

Figure 2.3: Models of electrical double layers in the neighborhood of the substrate surface [13].

2.4.1.1 The dynamic hydrogen bubble template (DHBT)

In the past fifteen years, electrochemistry research groups have built on the successes of synthesizing electronic materials such as semiconductors, alloys and layered composites, and developed new electrochemical tools for engineering nanofabrication. The electrochemical processes employed in nanofabrication are subdivided as anodic, cathodic and open-circuit processes. The importance of high specific surface area materials in catalysis and other surface confined processes cannot be over emphasized. Cost factor in using noble metals as catalyst drives the quest to design highly porous materials that guarantee economical use; hence perpetually evolving the science and technology aimed at understanding the parameters and controlling the morphology during fabrication of such materials.

At sufficient cathodic overpotential, H^+ is reduced to H_2 giving rise to bubbles on the surface of the electrode, where the metal is being deposited. The growth of metal occurs around these bubbles, maximizing the specific surface area by the formation of macro pores. This hydrogen bubbling can be applied as a template for versatile, simple and efficient deposition of dendritic foam growth structures [14].

Since the first detailed studies on copper, the method has been extended to synthesis of bimetallic films and a number of post deposition synergistic effect, and to tune activity of metals for application in catalysis.

2.4.1.1.1 Mechanism and experimental consideration

Though the precise mechanism varies depending on electrode material and conditions, the generation of gas bubbles generally involves three steps: nucleation, growth and detachment. Due to the high overpotential used in the template, the solution near the electrode is super saturated with hydrogen, resulting in heterogeneous nucleation. As the bubble grows during its residence time on the substrate, the contact angle decreases until it detaches. The generated hydrogen gas either diffuses into the bulk

solution, or fluxes to the liquid-gas interface of a bubble and coalesces. An illustration of the method is shown in figure 2.4.

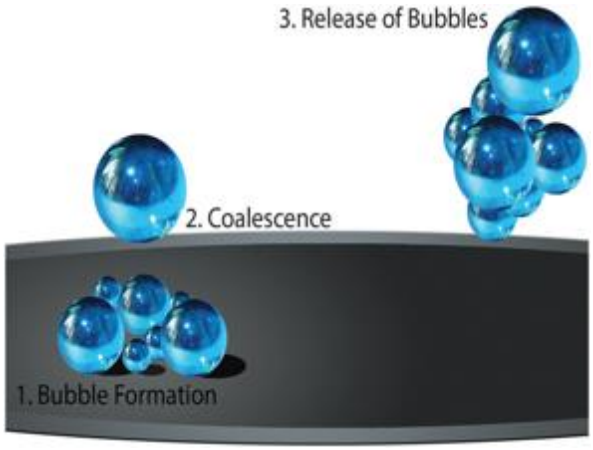

Figure 2.4: Schematic showing the bubble life cycle in the dynamic hydrogen bubble template [14].

The interaction between the interfacial tension in the 3-phase system (electrode/electrolyte/gas) is quite complex and not fully understood yet, hence tailoring of experimental parameters are undertaken in line with some general rules for bubble behavior.

2.4.1.1.2 Application in Synthesis of Bimetallic surfaces

A key merit of the DHBT is that it opens up scope for improvements in catalytic processes by leveraging synergistic effects in tuning activity. The synthesis of bimetallic surfaces can be classified as follows:

a. **Electrodeposited on top:** this involves depositing on top of a template previously fabricated by the DHBT method. A variety of reasons have been cited for adopting the two-step deposition approach rather than a direct electrodeposition approach, an observed common motivation is mechanical adhesion of the structure to the surface. Exploiting a well-studied system such as copper, the desired pore structure may be achieved. This method has been extensively applied with Ni, and Si in water electrolysis, and Li-ion batteries applications.

b. **Co-electrodeposition:** In this method, two or more metallic salts are dissolved in solution before electrodeposition, to give rise to a bimetallic honeycomb like material. In this method, altering the concentration of solutes in the deposition solution is a direct means of controlling the composition of the electrodeposits, as the high overpotential employed in the DHBT may eliminate all kinetic barriers that may hinder growth of any individual element and limit the reduction of metal species to diffusion-controlled cases.

c. **Galvanic replacement:** This method is employed to aid the conversion of monometallic materials into bimetallic ones. This method proceeds by virtue of the electrochemical potential difference of a related redox reaction where dissolution (oxidation) of the substrate occurs as one-half reaction, while deposition (reduction) of ions of a different metal occurs as the other half. Usually, the process alters the nanoscale morphology, with slight increases in dimensions due to the additive effect of electroless plating. Spontaneous decoration is similar

to galvanic replacement and differs only in that the immersion is done under open circuit potential conditions.

2.5 Sodium borohydride as a hydrogen carrier

The hydrolysis of sodium borohydride yields pure hydrogen, the rate of hydrogen production is a key consideration in the design of engineering applications. As hydrolysis proceeds, borates are formed, leaving the solution more basic and consequently retarding the generation rate. By employing catalysts in a buffered solution, this rate can be improved and controlled. Many organic and inorganic acids have been found to effectively accelerate the hydrolysis reaction, however the reaction often turned out uncontrollable. In this respect, transition metal catalysts like Ni and Cobalt (Co) have found some success.

The catalytic performance of non-noble metal based catalysts like Ni, and Co, prepared by a vast range of techniques like electroless reduction and in various structural forms like powders, oxides or borides for the hydrolysis of borohydride have been reported [15–18]. However, study of the synergistic effect of electrodeposited Nano porous 3D foams on a stainless-steel substrate is limited.

The stability and activity of Cu-Co foams as catalysts for sodium borohydride hydrolysis were recently reported [17], where the $Cu_{85}Co_{15}$ alloy performed optimally, as a result of modified morphology and electronic activity of the poor performing Cu_{100} and satisfactory performing Co_{100}.

2.5.1 Effect of $NaBH_4$ and NaOH concentrations

Investigations by Liu et al. on the relations of hydrogen generation rate with temperature evidenced a zero-order reaction kinetics, in agreeance with earlier reported observations on metal borides. However, they also reported that change in the initial concentration of borohydride slightly affected the generation rate and ascribed the phenomenon to influence on the catalyst; with decreased rate for less than 0. wt.% borohydride and no noticeable effect for higher concentrations. Sodium hydroxide concentrations of less than 20 wt.% showed no effect on hydrogen generation rate, upwards of 30 wt.%, the hydrogen generation rate deviated from the characteristic straight line, the observed phenomenon was explained by decreased water activity [16].

Table 2.1: Properties and performance of different Ni & Co catalysts in borohydride hydrolysis.

Catalyst	**Specific surface area (m^2g^{-1})**	**H_2 generation rate (293K) ($mLmin^{-1}g_{catalyst}^{-1}$)**	**Activation energy ($kJmol^{-1}$)**
Ni powder	1.98	19.5	-62.7
Co powder	1.15	126.2	-41.9
Raney Ni	-	228.5	-50.7
Raney Co	-	267.5	-53.7
Raney $Ni_{50}Co_{50}$	-	648.2	-52.5

3 EXPERIMENTAL PROCEDURE

3.1 Substrate Preparation

AISI 304 stainless steel substrates were used and were prepared for electrodeposition with the following steps:

i. Polishing with the LaboPol-25 machine with P600 silica carbide abrasive paper under flowing water.

Figure 3.1: Substrate Polishing.

ii. The samples were then soaked in acetone and placed in an ultrasonic machine for about 3 minutes to degrease the surface.

iii. The samples were then air dried and weighed.

3.2 Solution Preparation

All reagents used were of analytical grade. Solutions were prepared with Millipore water, at room temperature with the molar concentrations shown in Table 3.1. Agitation with a magnetic stirrer was used to aid dissolution of solution IV. 1.5M H_2SO_4 and 1M HCl were added to binary and ternary foams of nickel, copper and Iron.

Table 3.1: Molar concentration of solutions for co-deposition.

Solution ID	$NiSO_4.6H_2O$	$CuSO_4.5H_2O$	$(NH_4)_2Fe(SO_4)_2.6H_2O$	NH_4Cl	$CoCl_2$	NaCl	$NiCl_2$
I	0.5	0.01	-	-	-	-	-
II	0.5	0.02	-	-	-	-	-
III	0.25	0.01	-	-	-	-	-
IV	0.1875	0.0075	0.375	-	-	-	-
V	0.01	0.005	0.25	-	-	-	-
VI	-	-	-	2	0.1	-	-
VII	-	-	-	1.5	0.03	0.05	0.07
		$CoO_4S.7H_2O$			H_3BO_3		
VIII	0.09	0.053	0.03	0.28	0.4	-	-

3.3 Electrodeposition

Electrodeposition was carried out in a two-electrode cell connected to a power source (Kikusui Electronics, Model PAB 32-3), with a platinum plate serving as counter electrode. The co-deposition of the metals was achieved in galvanostatic mode over 1.55 cm^2 area of the substrate at 3A for 180 seconds for sample IDs I-V [19], while sample VI-VIII were at 1 $A.cm^{-2}$ for 90seconds, except for VIII which was for 180seconds. Each electrode was gently but thoroughly rinsed with Millipore water, dried with a jet of air, weighed and stored in airtight plastic vials for testing.

Figure 3.2: DHBT electrodeposition.

3.4 Characterization

Morphology and composition of the metallic foams were evaluated by scanning electron microscopy (SEM, Hitachi S2400) and energy dispersive X-ray spectroscopy (EDS, Rontec standard detector), respectively.

3.5 Electrochemical Techniques

There are three broad categories in electrochemical analysis, namely: chronopotentiometry; which involves measuring the electrode potential with time, chronoamperometry; where the cells current is measured over time and Voltammetry; measuring the cells current with the change of the potential value.

3.5.1 Voltammetry

The study of current (I) as a function of a potential (E) scan is voltammetry, the plot of I = f(E) is called a voltammogram. It is employed in the investigation of half-cell reactivity of an analyte.

3.5.1.1 Cyclic voltammetry

This technique involves sweeping across a potential range, and reversing the direction of the sweep after the upper limit is reached. Thus, reversing the electrochemical reaction for reversible processes. The characteristics of the voltammograms for reversible processes are:

- The ratio of peak current is unity.
- The positions of peak voltage are not functions of the voltage scan rate.
- The peak currents are functions of the scan rate square root.

The characteristic voltammogram recorded depend on several factors which include:

- The potential scan rate
- The rate of the electron transfer reactions
- The reactivity of the species

Linear scan voltammetry in principle refers to half (forward/backward) operation of cyclic voltammetry. The oxidation of $NaBH_4$ is irreversible. Therefore, the current peaks do not occur at the same voltage. Analyzing the variation of peak position as a function of scan rate, we can gain information on the estimate of the anodic charge transfer coefficient.

The electrochemical studies were carried out using a PAR 273A potentiostat (Princeton Applied Research, Inc.) connected to a dedicated computer with PowerSuite software installed. The setup was a three-electrode cell with a platinum mesh (Johnson Matthey) and a saturated calomel electrode (SCE) from Hanna instruments, serving as counter and reference electrodes, respectively. Hence, all potentials recorded in this study are relative to SCE reference.

Figure 3.3: Electrochemical analysis using a potentiostat.

Preceding the tests, an analyte solution of 0.03 M $NaBH_4$ (98%, Merck) was prepared in a 2M NaOH solvent from AnalaR NORMAPUR of 99% purity. The catalysts were subjected to chronoamperometric runs to reduce any surface oxides, followed by cyclic voltammetry studies, conducted for scan rates in the range of 5-500 mV s^{-1} for each catalyst.

3.6 Borohydride hydrolysis

3.6.1 Inverted Burette method

Each of the foam was placed in turns in a 500mL conical flask fitted with a 12mL capacity syringe containing freshly prepared borohydride solution. The flask is sealed to avoid gas leakage and set up with an inverted burette filled with water according to figure 3.5. The syringe is then emptied unto the foam surface and the timer is started. As the reaction proceeds, the hydrogen gas rises and the change in water level is recorded against time.

Figure 3.4: Inverted burette setup for borohydride hydrolysis.

3.6.2 Gas meter method

The amount of generated hydrogen was measured by using MilliGascounter (Ritter), whose cross-sectional view is shown in figure 3.6. In a typical measurement, the 15mL reaction solution containing 5 wt.% $NaBH_4$ and 0.4 wt.% NaOH is placed in an airtight flask fitted with an outlet for collection of produced H_2 gas, connected with the digital gas flowmeter. The foam is placed in the solution with a thermostatic temperature (60 °C) to initiate hydrolysis reaction of sodium borohydride.

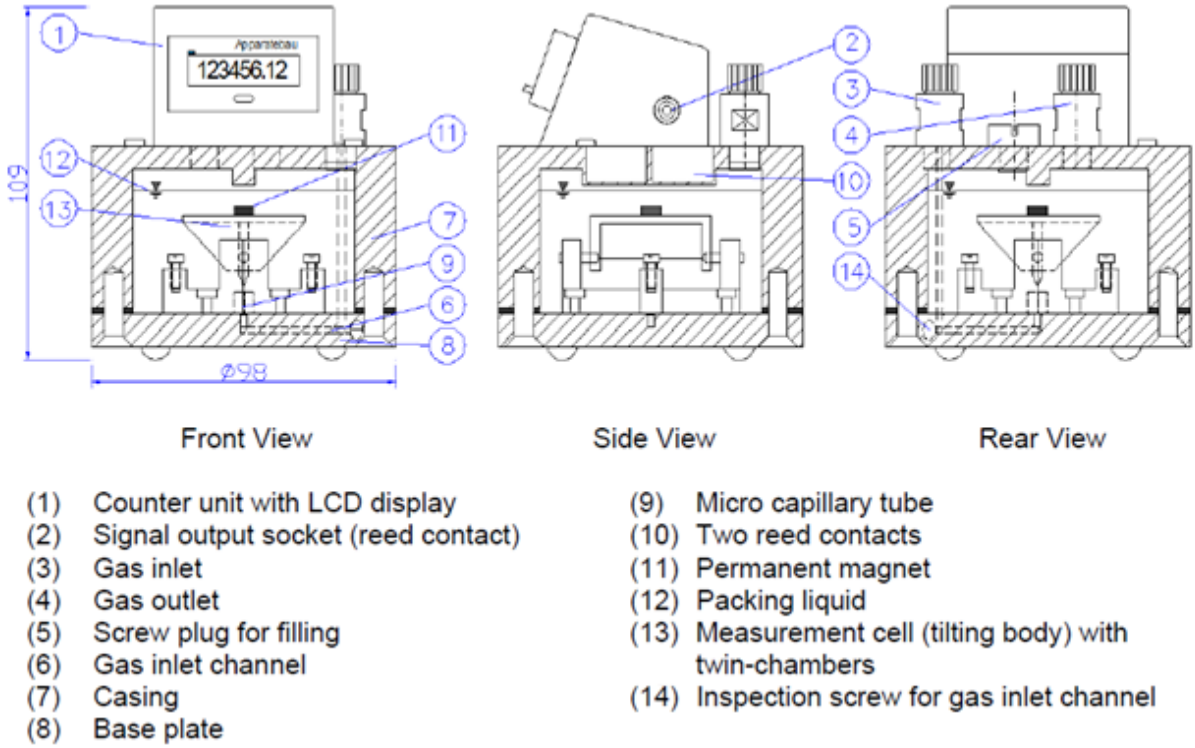

Figure 3.5: Cross-sectional view of digital gas meter (MilliGascounter).

4 RESULTS AND DISCUSSION

4.1 Deposition of Metallic Foams

Table 4.1 contains the mass deposited for each foam composition from the solutions under the conditions described in the experimental procedure.

Table 4.1 Mass of catalyst deposited.

Solution ID	Foam Composition (atomic wt.%)	Mass of catalyst / g	
I	$Ni_{52}Cu_{31}O_{17}$	0.0113	0.0143
II	$Ni_{34}Cu_{37}$	0.019	0.0178
III	$Ni_{36}Cu_{46}O_{16}$	0.009	0.0085
IV	$Ni_{14}Cu_{26}Fe_{41}O_{18}$	0.0097	0.0102
V	$Ni_{4}Cu_{48}Fe_{30}O_{12}$	0.0015	0.0023
VI	Co_{100}	0.0198	0.0195
VII	$Ni_{65}Co_{35}$	0.0253	0.025
VIII	$Ni_{62}Co_{24}Fe_{14}$	0.0129	0.0245

4.2 Morphological Characterization

Using SEM, the morphology of the electrodeposited metallic foams was characterized (Figures 4.1 to 4.8). High cathodic current densities employed during electrodeposition resulted in continuous bubbling of H_2, which limited the free volume available for metal growth by blocking the diffusion of active species, giving rise to three dimensional foam-like morphologies with randomly distributed micrometric and nanometric pores, obtained under mass transfer conditions [19].

I used EDS to determine the chemical compositions and loadings for all foam samples. The intended loadings were successfully achieved with notably small presence of impurities like sulfur and chromium in a few cases.

The magnification and corresponding accelerating voltage parameters for SEM analysis are as tabulated below:

Table 4.2: Parameters for SEM analysis.

SCALE	MAGNIFICATION	ACCELERATING VOLTAGE
1µm	20000x	15kV
5µm	5000x	20kV
30µm	1000x	20kV
50µm	500x	20kV
100µm	200x	20kV

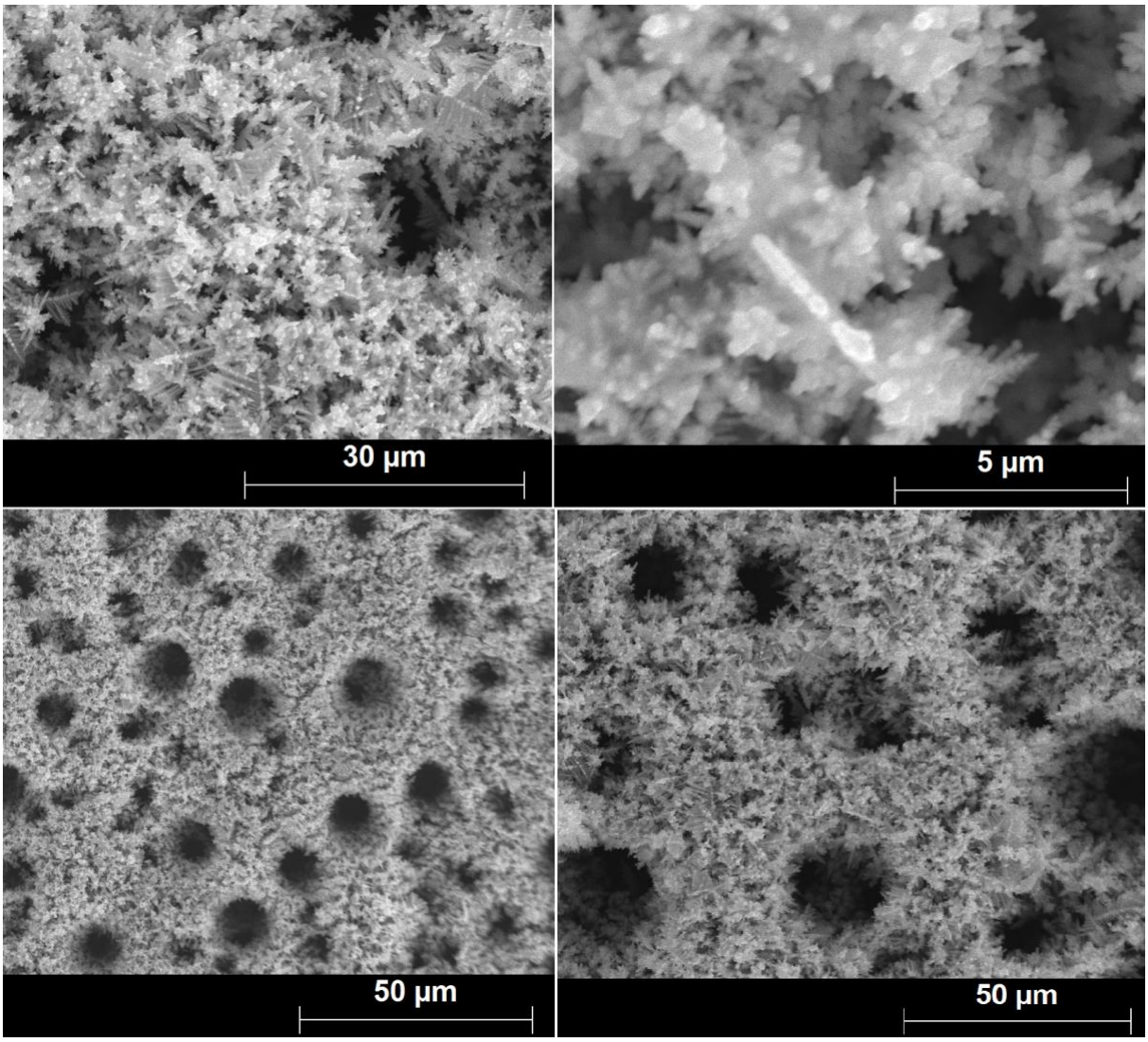

Figure 4.1: SEM image of $Ni_{52}Cu_{31}O_{17}$ metallic foam.

Table 4.3: Chemical composition of $Ni_{52}Cu_{31}O_{17}$ metallic foam, as determined by EDS.

Element	[norm. wt.%]	[norm. at.%]	Error in wt.% (1 Sigma)
Nickel	57.6	51.9	1.5
Copper	37.3	31.0	1.1
Oxygen	5.2	17.1	1.5
	100	100	

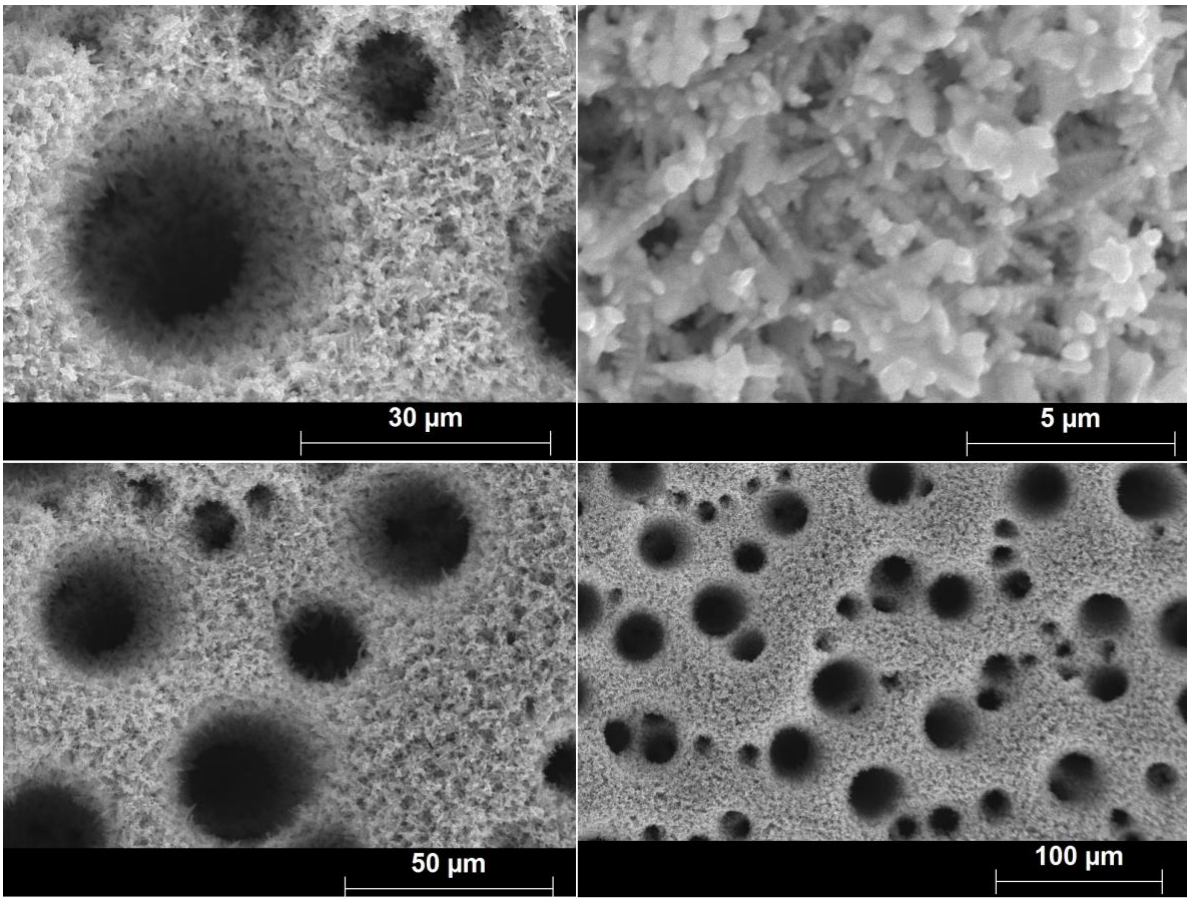

Figure 4.2: SEM image of $Ni_{34}Cu_{37}$ metallic foam.

Table 4.4: Chemical composition of $Ni_{34}Cu_{37}$ metallic foam as determined by EDS.

Element	[norm. wt.%]	[norm. at.%]	Error in wt.% (1 Sigma)
Nickel	41.0	33.8	1.1
Copper	48.4	36.8	1.3
Oxygen	8.8	26.6	2.0
Sulfur	1.9	2.8	0.2
	100	100	

A clear observation in the $Ni_{34}Cu_{37}$ foam (figure 4.2) in which the fractional percentage of Ni is reduced from 52% in $Ni_{52}Cu_{31}$ foam (figure 4.1), is an enhanced circular definition of the pores due to less dendritic ramifications of the pore walls, increased pore sizes and reduced surface pore density.

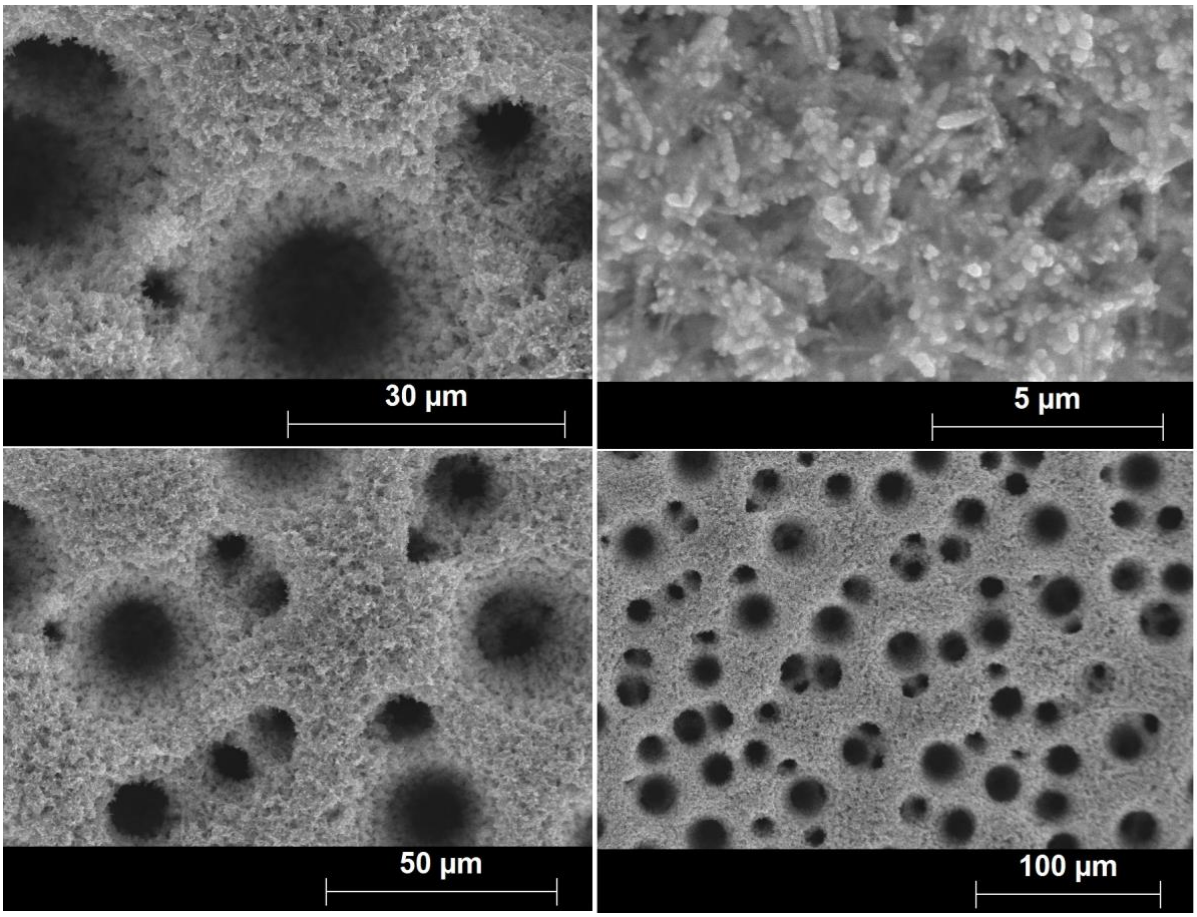

Figure 4.3: SEM image of $Ni_{36}Cu_{46}O_{16}$ metallic foam

The interconnectivity of the pores seemed to improve and less dendritic ramifications are observed with increasing fractional composition of copper in $Ni_{36}Cu_{46}$ foam (figure 4.3). The density of surface pore also increases, however, the overall porosity of three-dimensional metallic foams depends not only on the pore density, but the voids in the pore walls as well [19], so it is impossible to ascertain the more porous foam without further measurements.

Table 4.5: Chemical composition of $Ni_{36}Cu_{46}O_{16}$ metallic foam as determined by EDS.

Element	[norm. wt.%]	[norm. at.%]	Error in wt.% (1 Sigma)
Nickel	39.0	35.9	1.2
Copper	54.2	46.1	1.6
Iron	1.7	1.7	0.1
Chromium	0.3	0.4	0.1
Oxygen	4.8	16.0	1.4
	100	100	

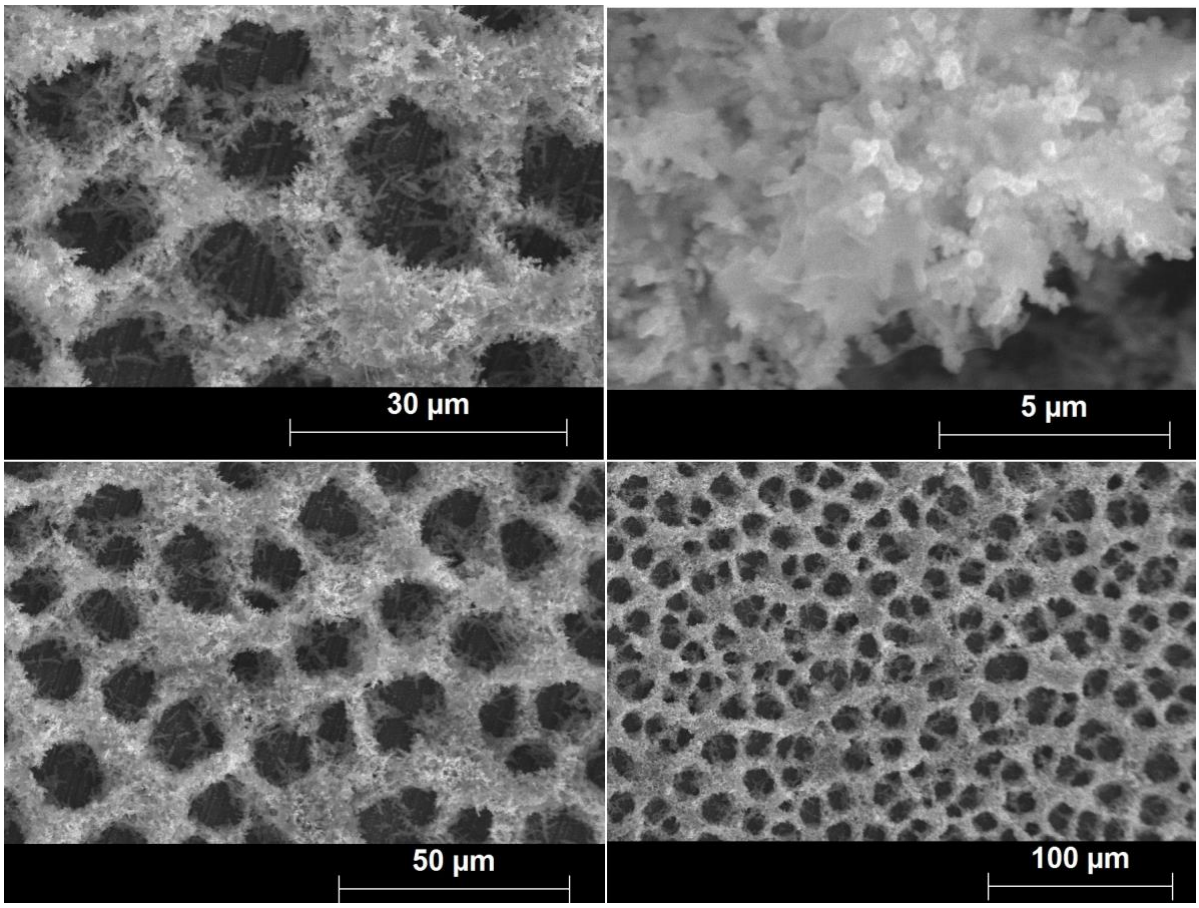

Figure 4.4: SEM image of $Ni_{14}Cu_{26}Fe_{41}O_{18}$ metallic foam.

The ternary foam samples (figures 4.4-4.5) containing nickel, copper, and iron, were generally characterized by a highly interconnected cross-linked structure, similar to a fisherman's net, with significantly increased surface pore density when compared with the bimetallic nickel-copper foams. The pore walls seem to retain the dendritic structure earlier described.

Table 4.6: Chemical composition of $Ni_{14}Cu_{26}Fe_{41}O_{18}$ metallic foam as determined by EDS.

Element	[norm. wt.%]	[norm. at.%]	Error in wt.% (1 Sigma)
Nickel	16.0	13.9	0.6
Copper	32.6	26.2	1.0
Iron	45.0	41.1	1.3
Chromium	0.7	0.7	0.1
Oxygen	5.7	18.0	1.7
	100	100	

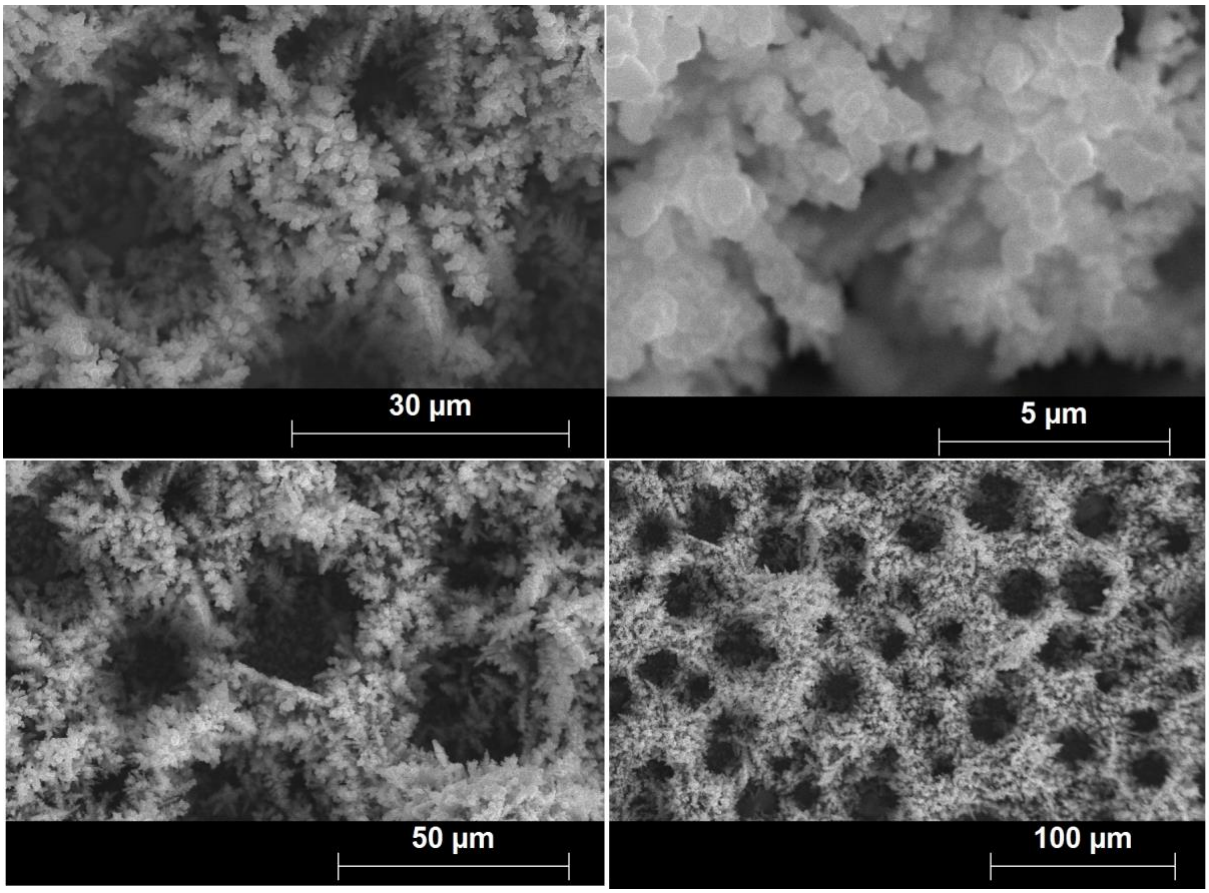

Figure 4.5: SEM image of $Ni_4Cu_{48}Fe_{30}O_{12}$ metallic foam.

The fractional percentage of nickel is reduced considerably, while that of copper is increased by ca. 50% and iron decreased by ca. 25% from $Ni_{14}Cu_{26}Fe_{41}O_{18,}$ as a result, there is notably a loss of grid like interconnectivity, reduction of the dendritic branches, larger pore size, and reduced surface pore density as compared to the ternary sample in figure 4.4.

Table 4.7: Chemical composition of $Ni_4Cu_{48}Fe_{30}O_{12}$ metallic foam as determined by EDS.

Element	[norm. wt.%]	[norm. at.%]	Error in wt.% (1 Sigma)
Nickel	4.1	3.8	0.2
Copper	55.8	47.8	1.5
Iron	30.4	29.6	0.8
Chromium	6.1	6.4	0.2
Oxygen	3.6	12.3	1.1
	100	100	

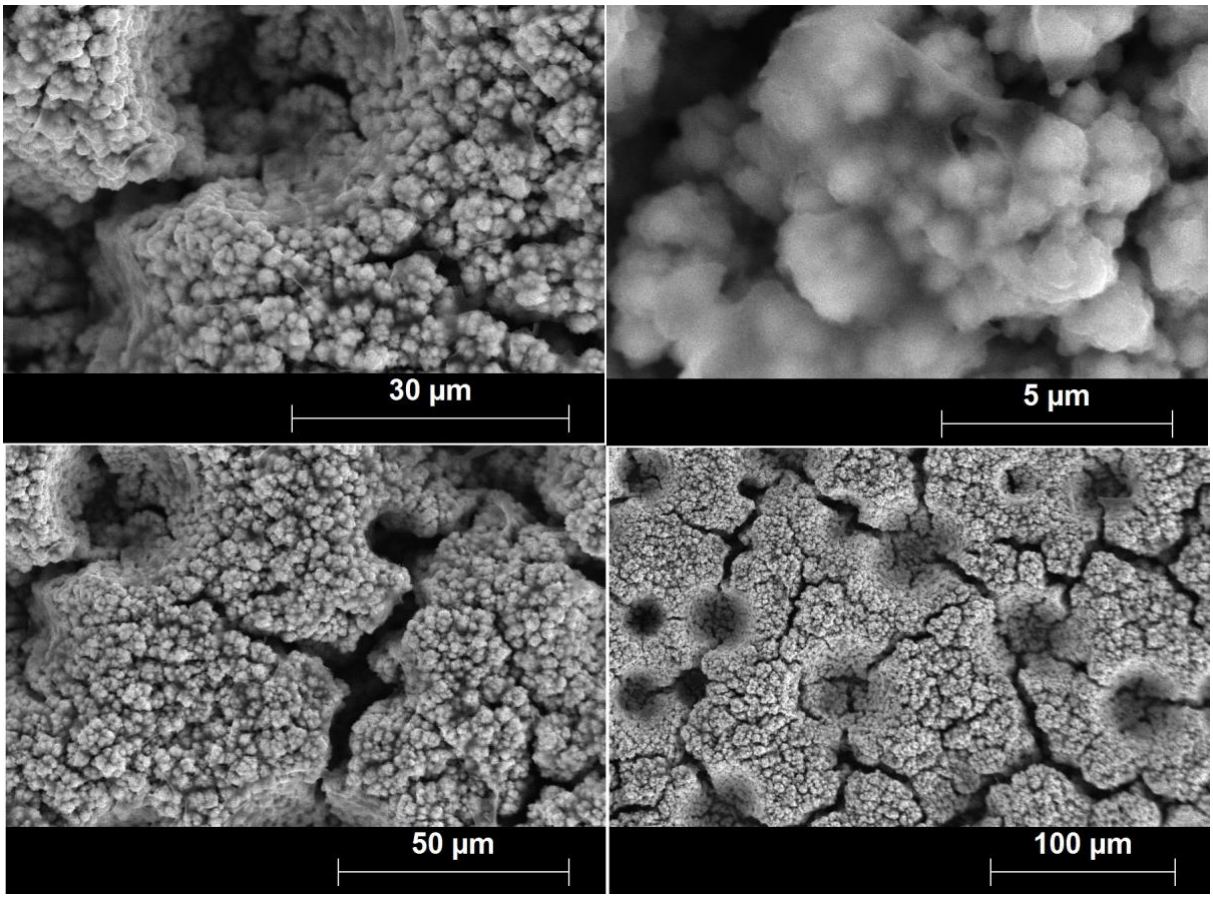

Figure 4.6: SEM image of Co_{100} metallic foam.

The pure cobalt foam shown in figure 4.6 was characterized by sparse, shallow, poorly interconnected and randomly distributed circular/crater shaped pores [20], the magnified insets reveal a densely packed pore wall with less ramified dendritic protrusions in comparison with nickel-copper foams.

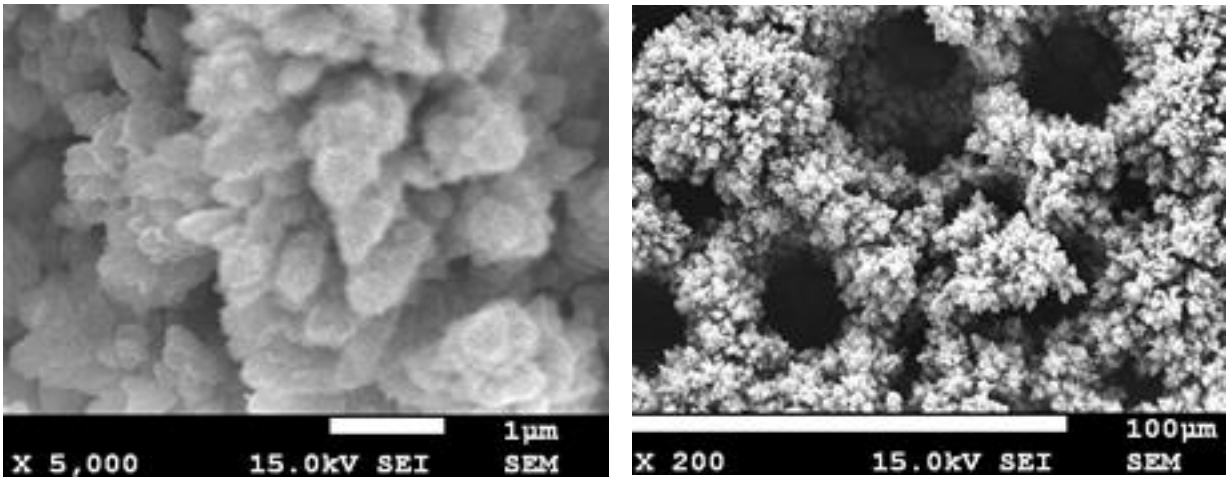

Figure 4.7: SEM image of $Ni_{65}Co_{35}$ metallic foam.

Co-depositing nickel with cobalt, eliminated the crater like pores earlier observed in purely cobalt foams, forming more circular pore definitions with improved pore volume (depth), and surface pore

density. The pore walls were more cauliflower like and showed no similarity with the previous dendritic structures seen.

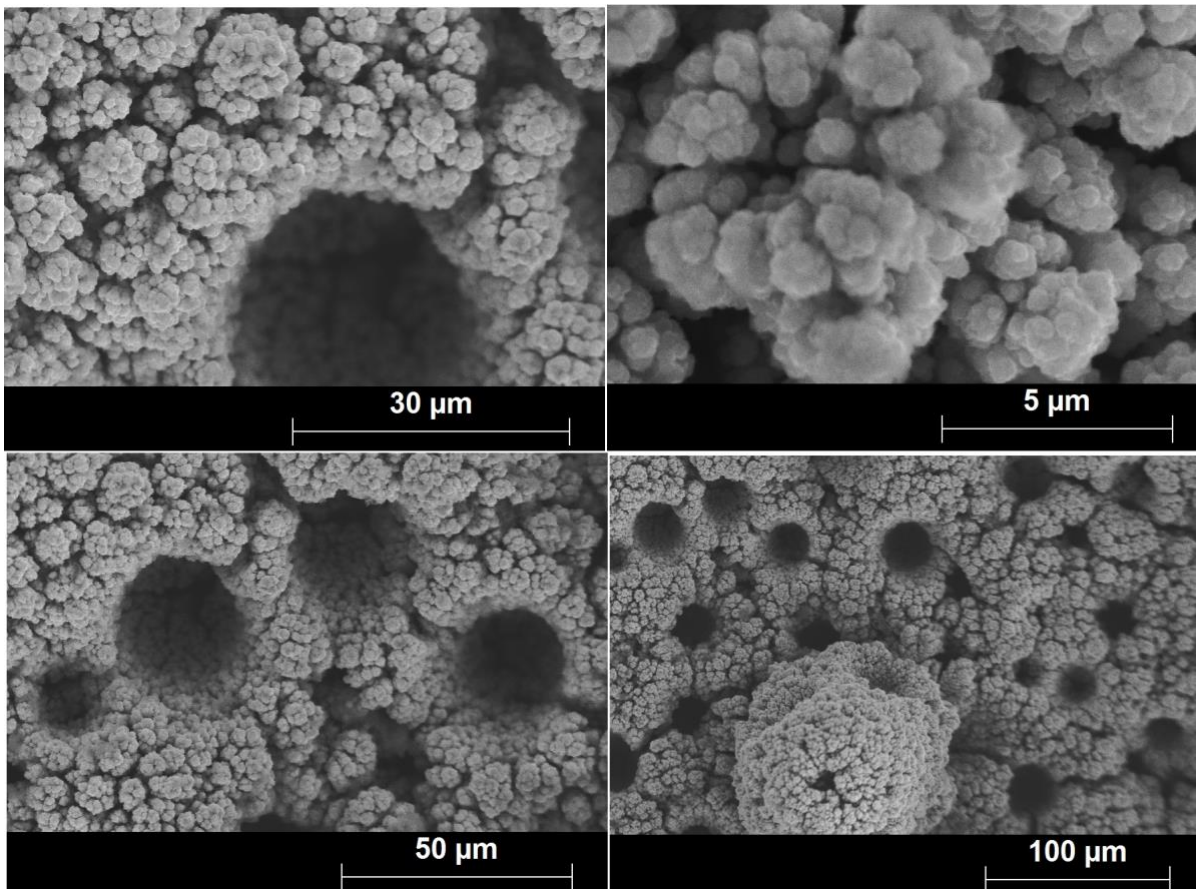

Figure 4.8: SEM image of $Ni_{62}Co_{24}Fe_{14}$ metallic foam.

The $Ni_{62}Co_{24}Fe_{14}$ shown in figure 4.8 above clearly retains the cauliflower like structure characteristic of Ni-Co foam discussed earlier, it appears that the introduction of iron, reduced the porosity as non-porous lumpy overgrowths are observed, with less surface pore density and interconnectivity.

Table 4.8: Chemical composition of $Ni_{62}Co_{24}Fe_{14}$ metallic foam as determined by EDS.

Element	[norm. wt.%]	[norm. at.%]	Error in wt.% (1 Sigma)
Nickel	62.6	62.2	2.1
Cobalt	24.4	24.1	0.9
Iron	13.0	13.6	0.5
	100	100	

4.3 Voltammetric Studies and Peak Analysis

Previous investigation on the electrochemical behavior of Ni-Cu foams, found their voltammograms depictive of pseudocapacitive behavior (i.e. storing charge from reversible redox reactions, couple redox peaks in the potential range of -0.2 to 0.8V were observed. The anodic peak corresponds to the oxidation of nickel and the cathodic peak to the corresponding reduction [19].

The mechanism of BOR at Ni based electrodes is inconclusive, making the peak assignment from voltammetric studies an arduous task. Tsionskii et al. suggested that BH_4^- is electrochemically inactive

at Ni electrodes in the region between 0 and 0.6V, hence anodic currents seen in that region stem from the oxidation of adsorbed H atoms from BH_4^- hydrolysis. On the contrary, Dong et al. concludes that borohydride hydrolysis does not take place at potentials less than 0 V, hence ascribing the peaks seen in the mentioned potential range to oxidation of hydrogen atoms adsorbed during the electrooxidation of borohydride [21]. The potential range used in this work has been limited to 0 V as the oxidation of borohydride can be hindered by the oxidation of the catalysts at more positive potentials [22]. Cyclic Voltammograms were recorded in 0.03 M $NaBH_4$ + 2 M NaOH by applying scan rates from 5 to 500 mV.s $^{-1}$ for all samples.

Figure 4.9-4.16 below shows voltammograms with varying scan rates and in alkaline control electrolyte (2M NaOH) for the metallic foams.

The shifts in peak potential value, E_p, for BOR with the scan rate, ν, is described by the following equation, assuming it occurs as a single-step irreversible process,

$$E_p = E^0 + \frac{RT}{(1-\alpha)n_aF}\left[0.78 + \ln\left(\frac{D^{\frac{1}{2}}}{k_s}\right) + \ln\left(\frac{(1-\alpha)n_aF\nu}{RT}\right)^{\frac{1}{2}}\right] \quad (4.1)$$

where E^0 is the formal potential (V), R is the universal gas constant (8.314JK^{-1}mol^{-1}), T is the temperature (K), α is the charge transfer coefficient, n_a is the number of electrons involved in the rate determining step, F is the Faraday constant (96485 C mol^{-1}), D is the diffusion coefficient of BH_4^- (cm^{2}s^{-1}), and k_s is the standard heterogeneous rate constant (cm s^{-1}).

The fraction of energy that goes to anodic oxidation reaction, termed the charge transfer coefficient, is dependent on the reaction involved and the electrode material. D, the diffusion coefficient of BH_4^- is determined from the following equation, valid for 2 M NaOH solution [21]:

$$D = 5.57 \times 10^{-3} exp\left(\frac{-15.2\times10^3}{RT}\right) \quad (4.2)$$

The variation of peak current density j_p with scan rate ν can be described by the modified Randles-Sevcik equation for irreversible processes shown below,

$$j_p = 2.99 \times 10^5[(1-\alpha)n_a]^{\frac{1}{2}} nCD^{\frac{1}{2}}\nu^{\frac{1}{2}} \quad (4.3)$$

Where C is $NaBH_4$ bulk concentration in mol.cm^{-3}, and all other symbols retain their definition.

4.3.1 Analysis for $Ni_{52}Cu_{31}O_{17}$ foam

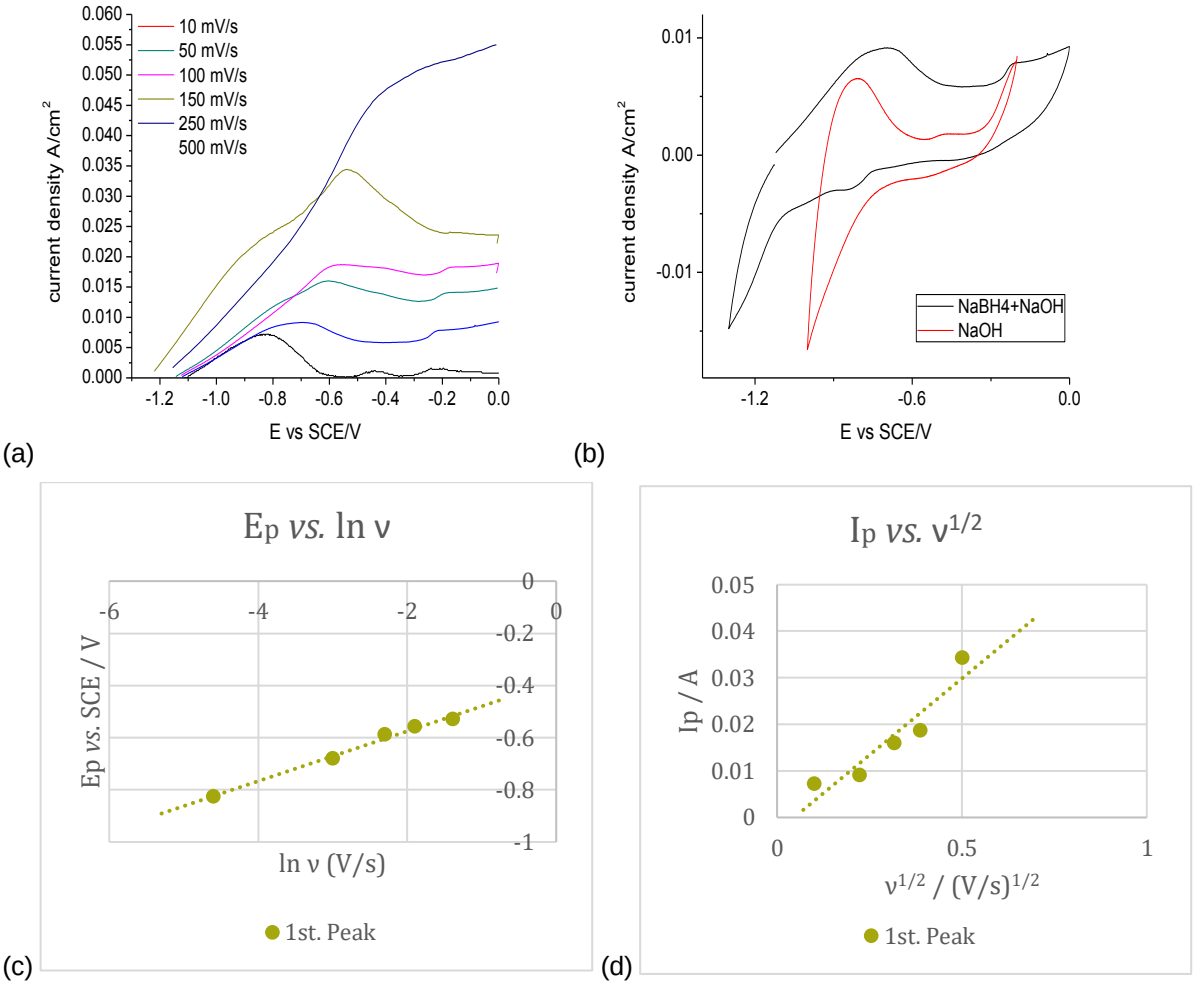

Figure 4.9: Voltammograms for $Ni_{52}Cu_{31}O_{17}$ (a) at different scan rates in 0.03 M $NaBH_4$ + 2 M NaOH, (b) at 50 mV.s^{-1} in the absence and presence of sodium borohydride, (c) resolution of α using plot of peak potential against logarithm of scan rate, (d) plot of Current against square root of scan rate used to estimate n.

A distinct peak registered at -0.7V is attributed to the oxidation of borohydride on this catalyst, this corresponds to a current of 9 mA.cm^{-2}. We can infer from the steeply rising curve in the control electrolyte that peaks seen at potentials greater than -0.3V are more likely associated with oxidation of the catalyst metals.

4.3.2 Analysis for $Ni_{34}Cu_{37}$ foam

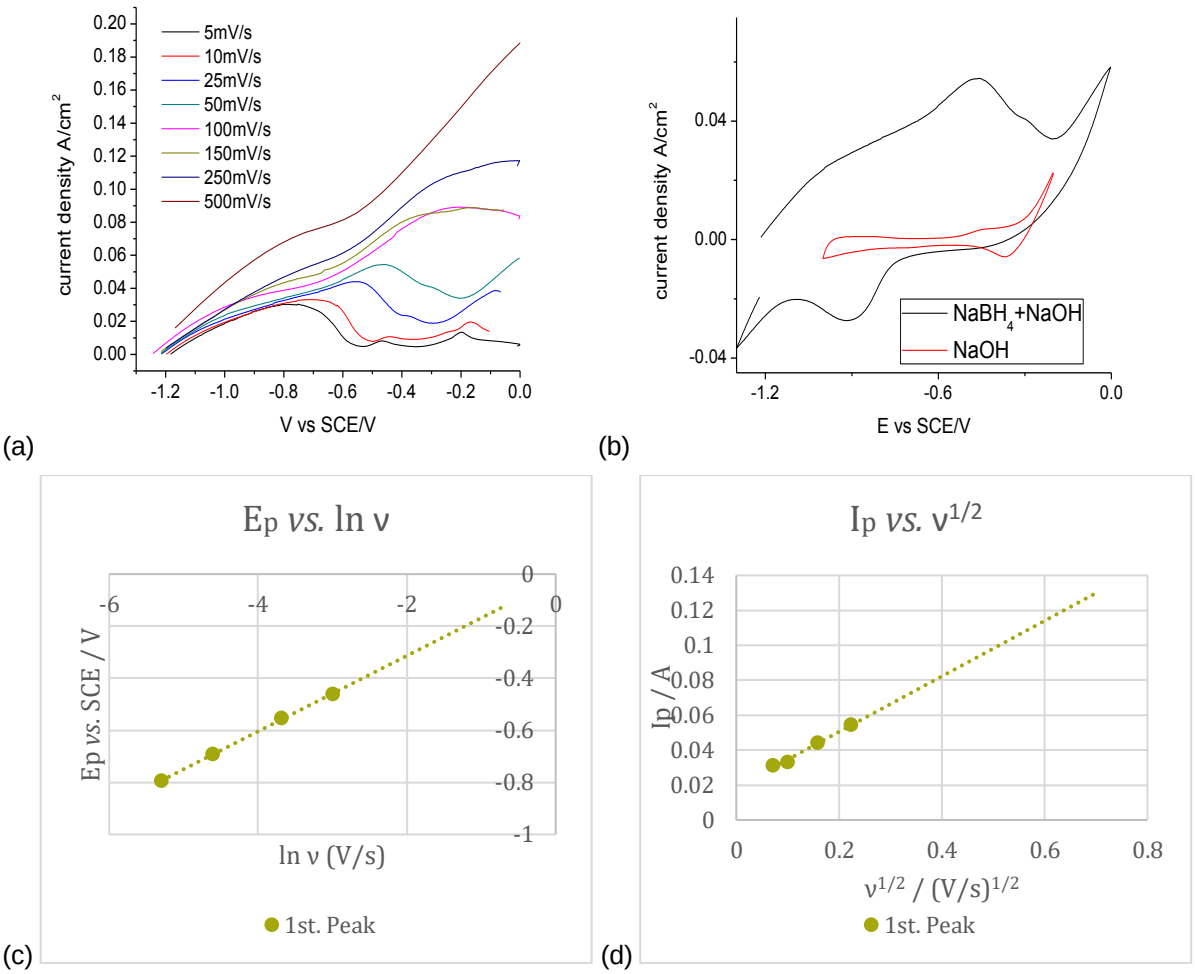

Figure 4.10: Voltammograms for $Ni_{34}Cu_{37}$ (a) at different scan rates in 0.03 M $NaBH_4$ + 2 M NaOH, (b) at 50 $mV.s^{-1}$ in the absence and presence of sodium borohydride (c) resolution of α using plot of peak potential against logarithm of scan rate (d) plot of Current against square root of scan rate used to estimate n.

Multiple peaks are seen in the -0.8 to -0.2 potential range, attributable to partial hydrolysis of BH_4^- and consequent oxidation of adsorbed H_2 atoms and BH_3OH^-, its hydrolysis products. The anodic peaks shift to the right with increasing scan rate, however, the peaks notable at potentials above -0.45 V disappeared as scan rate increased. The more consistent peak series that corresponds to -0.45 V and 54 $mA.cm^{-2}$ in the 50 $mV.s^{-1}$ scan rate, is assigned to the borohydride oxidation.

4.3.3 Analysis for $Ni_{36}Cu_{46}O_{16}$ foam

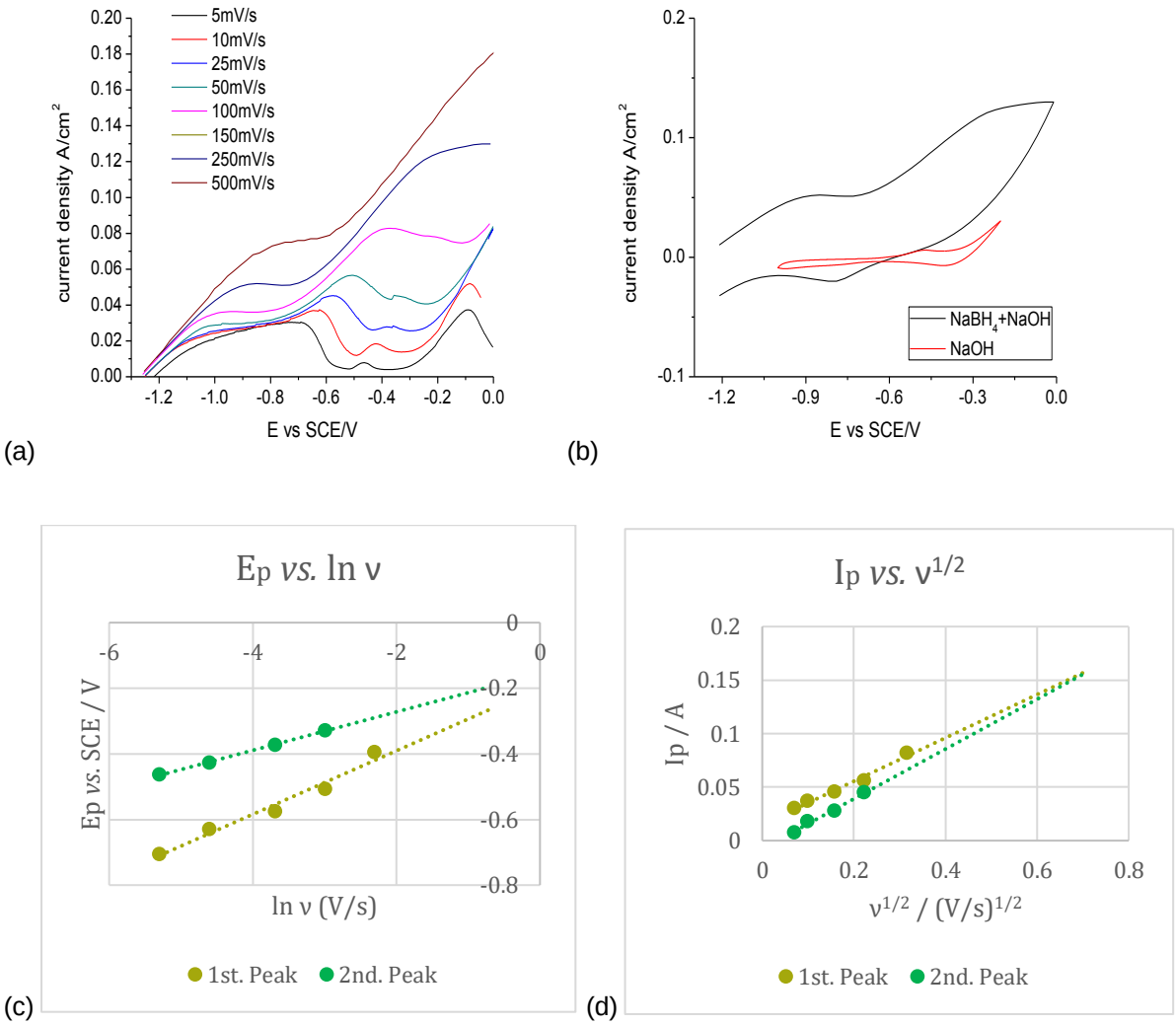

Figure 4.11: Voltammograms for $Ni_{36}Cu_{46}O_{16}$ (a) at different scan rates in 0.03 M $NaBH_4$ + 2 M NaOH, (b) at 50 $mV.s^{-1}$ in the absence and presence of sodium borohydride (c) resolution of α using plot of peak potential against logarithm of scan rate (d) plot of Current against square root of scan rate used to estimate n.

From the cyclic voltammogram of the control electrolyte we can infer that oxidation of catalyst components will take place at potentials above -0.3V, the multiple peaks observed at lower potentials are analyzed for borohydride hydrolysis. A current density of 50 $mA.cm^{-2}$ in the 50$mV.s^{-1}$ scan rate is recorded at -0.5V, in consistency with the Ni-Cu foam in figure 4.10.

4.3.4 Analysis for $Ni_{14}Cu_{26}Fe_{41}O_{18}$ foam

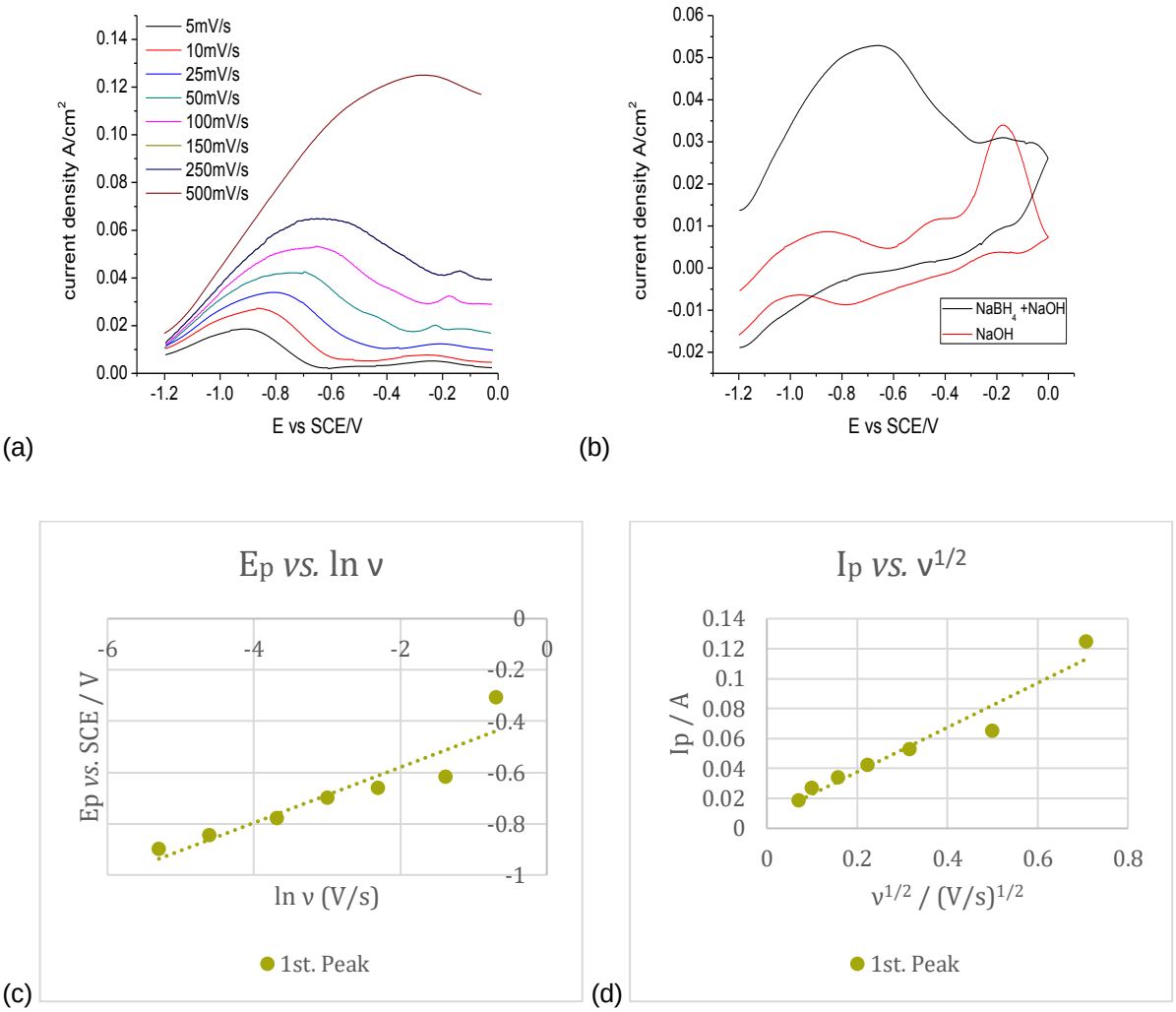

Figure 4.12: Voltammograms for $Ni_{14}Cu_{26}Fe_{41}O_{18}$ (a) at different scan rates in 0.03 M $NaBH_4$ + 2 M NaOH, (b) at 50 $mV.s^{-1}$ in the absence and presence of sodium borohydride (c) resolution of α using plot of peak potential against logarithm of scan rate (d) plot of Current against square root of scan rate used to estimate n.

Considerable noise was observed with the voltammogram of the ternary foam. The peak at -0.7V does not appear in the control experiment and forms our basis for analysis of borohydride oxidation at this potential for the $Ni_{14}Cu_{26}Fe_{41}$ foam. A coinciding peak is seen at the less negative potential of -0.2V between the experiment and the control. This could be due to partial oxidation of the adsorbed hydrogen, and possibly some of the catalyst metal.

4.3.5 Analysis for $Ni_4Cu_{48}Fe_{30}O_{12}$ foam

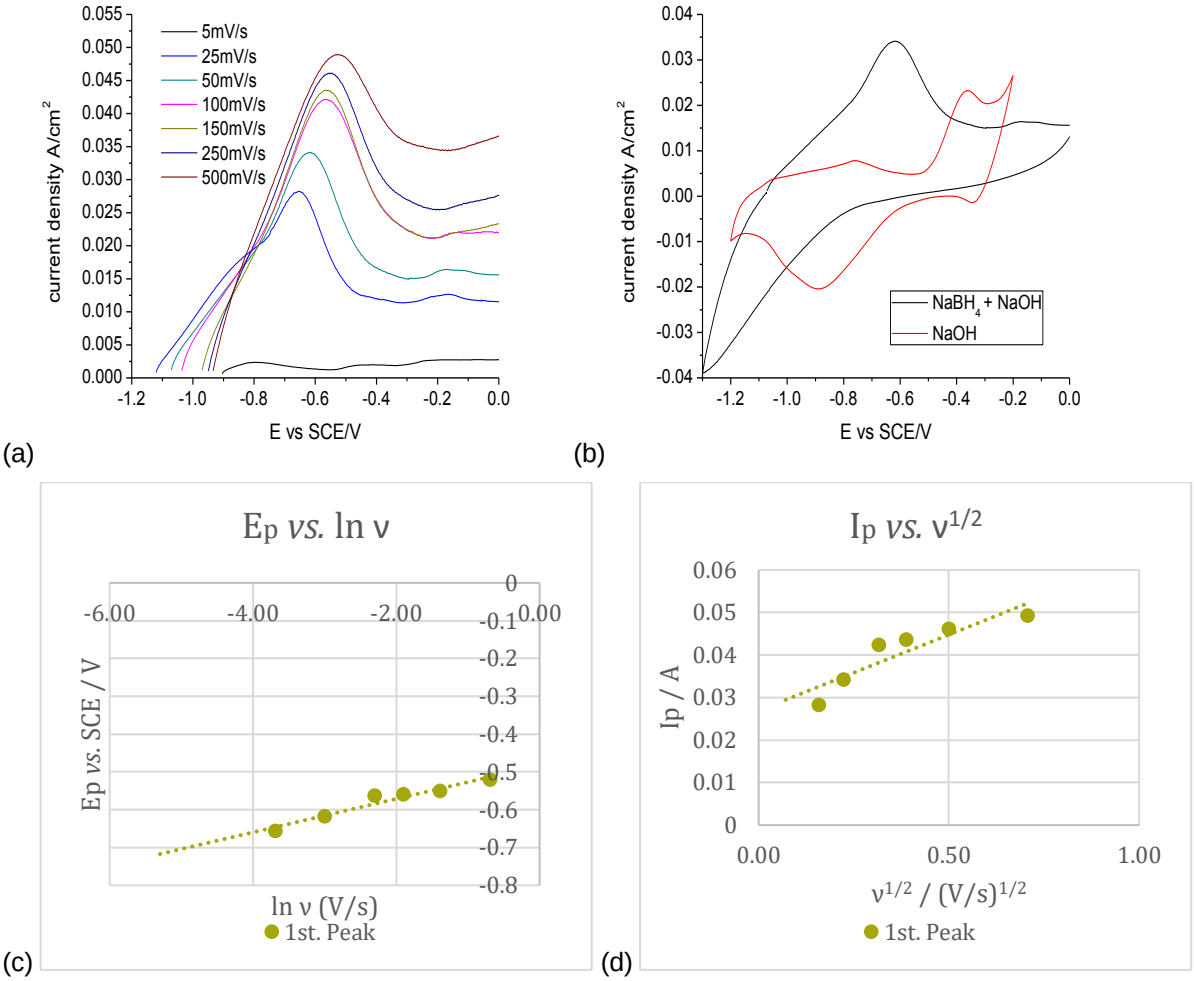

Figure 4.13: Voltammograms for $Ni_4Cu_{48}Fe_{30}O_{12}$ (a) at different scan rates (b) at 50 $mV.s^{-1}$ in the absence and presence of sodium borohydride (c) resolution of α using plot of peak potential against logarithm of scan rate (d)plot of Current against square root of scan rate used to estimate n.

A current density of 32.5 $mA.cm^{-2}$ is recorded at a 50 $mV.s^{-1}$ scan rate at a potential of -0.6V, the control experiment showed a different voltammogram, with a slight peak at -0.75V appearing and a more distinct peak at -0.3V, both in the oxidation potential range of Iron (II) and Copper respectively.

4.3.6 Analysis for Co_{100} foam

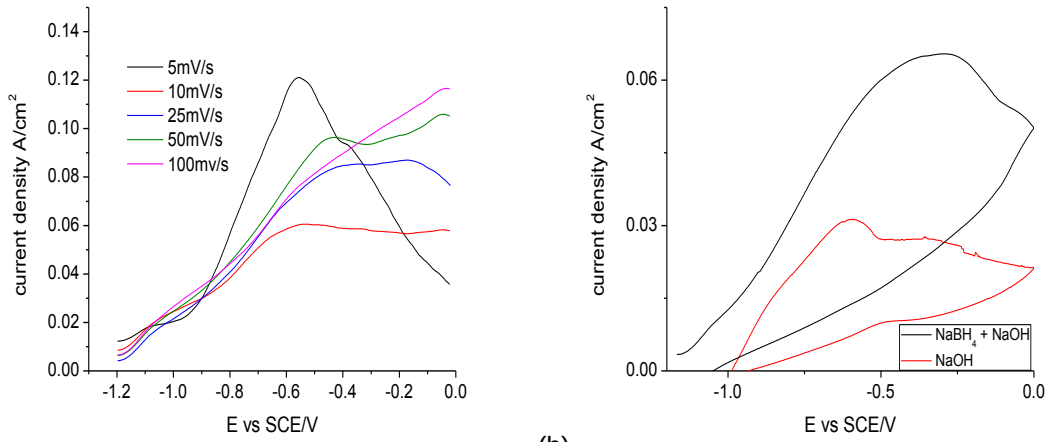

Figure 4.14: Voltammograms for Co_{100} (a) at different scan rates in 0.03 M $NaBH_4$ + 2 M NaOH (b) at 50 $mV.s^{-1}$ in the absence and presence of sodium borohydride.

The voltammogram obtained for the pure cobalt foam shown in figure 4.14 behaves distinctively differently from the observed trend, the identical nature of the curves obtained in the control experiment would lead to the suggestion that oxidation of catalyst material is occurring, this is supported by the high peak obtained during the slow scan rate of 5 $mV.s^{-1}$, which becomes less at 10 $mV.s^{-1}$, and non-existing beyond 50 $mV.s^{-1}$.

4.3.7 Analysis for $Ni_{65}Co_{35}$ foam

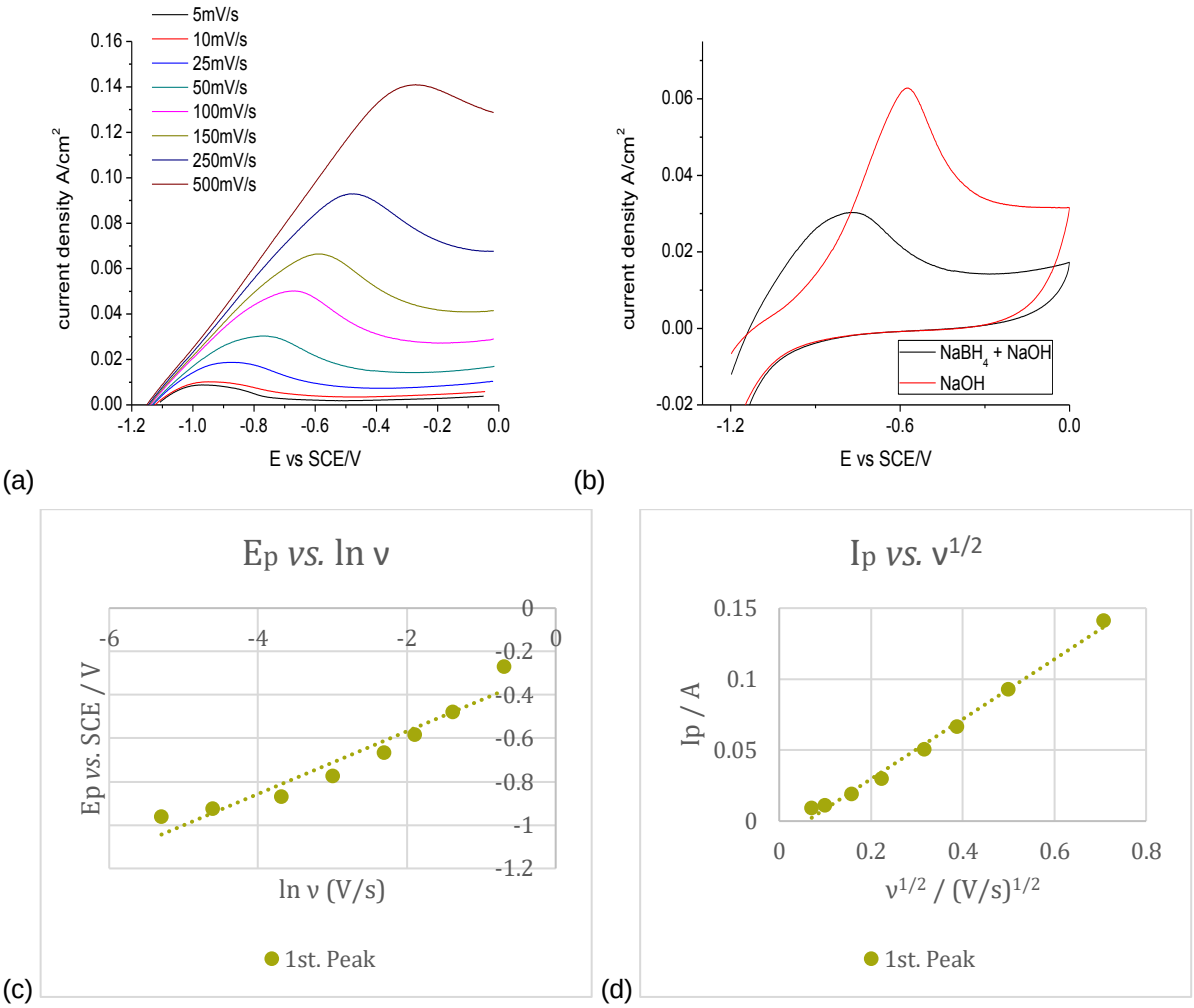

Figure 4.15: Voltammograms for $Ni_{65}Co_{35}$ (a) at different scan rates in 0.03 M $NaBH_4$ + 2 M NaOH, (b) at 50 $mV.s^{-1}$ in the absence and presence of sodium borohydride (c) resolution of α using plot of peak potential against logarithm of scan rate (d)plot of Current against square root of scan rate used to estimate n.

Higher peak was recorded for the control experiment in NaOH, suggesting oxidation of catalyst material. The reduced peak noticed in the experiment in the presence of sodium borohydride; which is a strong reducing agent could be explained as the suppression of catalyst material oxidation.

4.3.8 Analysis for $Ni_{62}Co_{24}Fe_{14}$ foam

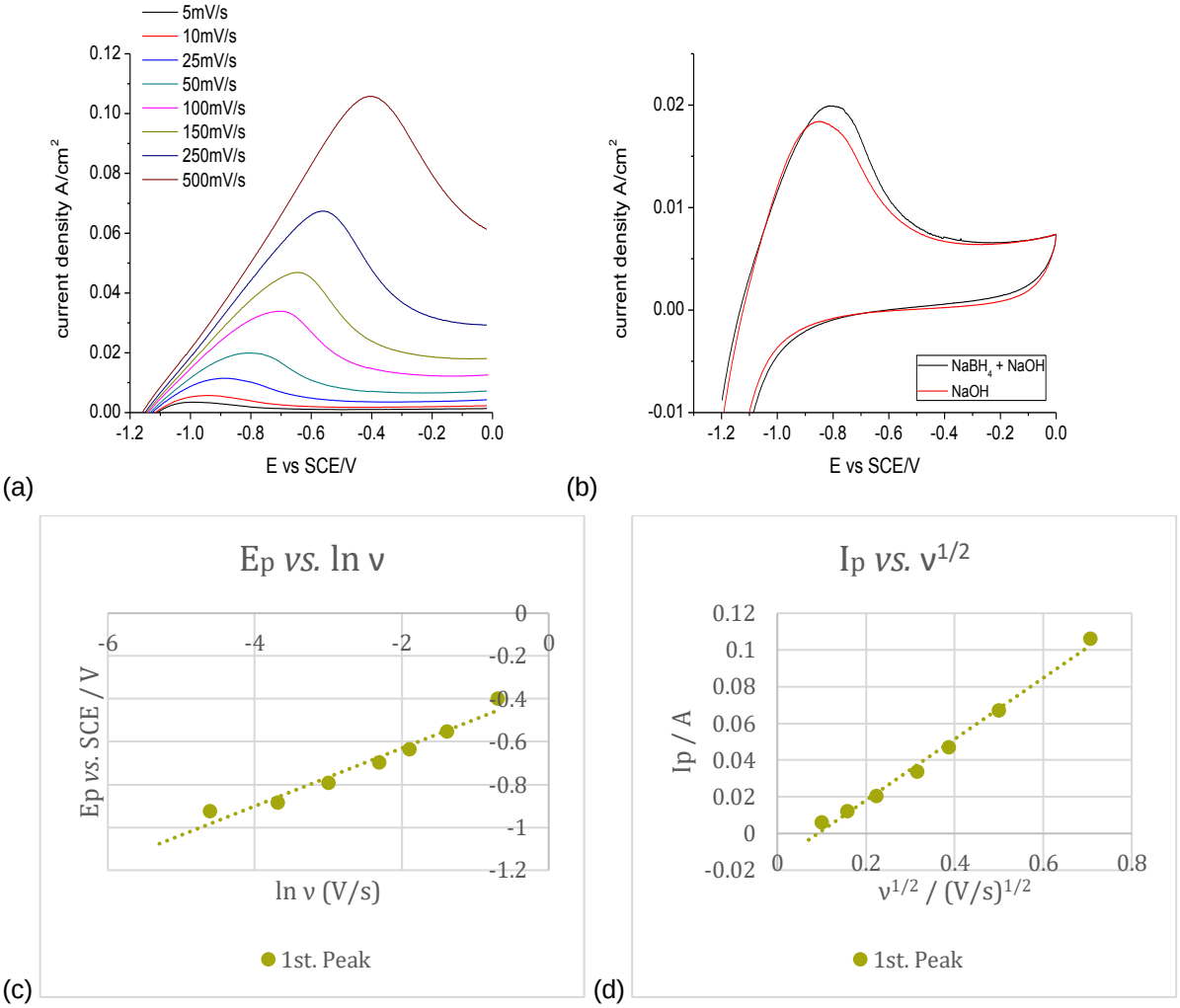

Figure 4.16: Voltammograms for $Ni_{62}Co_{24}Fe_{14}$ (a) at different scan rates (b) at 50 $mV.s^{-1}$ in the absence and presence of sodium borohydride (c) resolution of α using plot of peak potential against logarithm of scan rate (d)plot of Current against square root of scan rate used to estimate n.

The superimposed voltammograms in figure 4.16 b. suggests the absence of borohydride hydrolysis. However, the peak analysis is conducted for the registered peaks to obtain kinetic data for the prevailing reaction on the foam surface in alkaline medium.

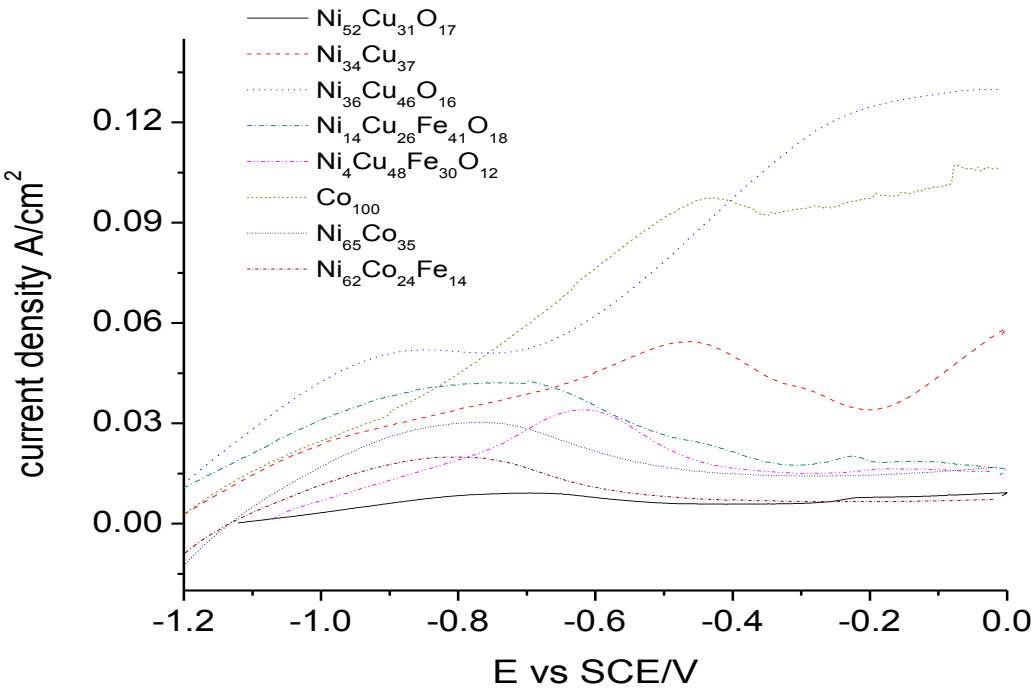

Figure 4.17: Comparison of all foam voltammograms at 50mVs^{-1}.

Table 4.8 summarizes the deductions from the peak analysis of the tested metallic foams towards borohydride electrooxidation.

Table 4.9: Summary of peak analysis for samples.

Foam composition	No. of electron transfer, n	Charge transfer coefficient	Maximum oxidation current density (mA·cm^{-2})	Maximum oxidation Current density per mass of catalyst (mA·g^{-1})
$Ni_{52}Cu_{31}O_{17}$	4.1	0.80	34.3	2882.35
$Ni_{34}Cu_{37}$	12.1	0.91	54.4	3022.22
$Ni_{36}Cu_{46}O_{16}$	12.6	0.87	82.0	9590.64
$Ni_{14}Cu_{26}Fe_{41}O_{18}$	9.8	0.88	124.7	13057.59
$Ni_{4}Cu_{48}Fe_{30}O_{12}$	1.5	0.71	49.2	28771.93
Co_{100}	-	0.81	97.0	7637.79
$Ni_{65}Co_{35}$	16.1	0.91	140.9	5774.59
$Ni_{62}Co_{24}Fe_{14}$	15.7	0.90	105.9	4394.19

4.4 Hydrogen evolution

The foams were tested for effect of NaOH concentration by conducting the experiment with different borohydride to NaOH concentrations, for a 4:1 molar ratio of NaOH to $NaBH_4$, the Co_{100} foam tended to deactivate as shown, however all other foams were stable.

Figure 4.18: Deactivated catalyst surface.

After several unsuccessful attempts on pure cobalt foam with varying molar ratios of borohydride to NaOH in the inverted burette method, some success was recorded with a 1:2 molar ratio in terms of foam stability and measurable hydrogen production volumes. 149.8 mL of hydrogen was recorded in 50 minutes, equivalent to 0.56 moles of H_2 per mole of $NaBH_4$.

The evolution of hydrogen was recorded over 5 cycles, activity of the foam decreased between cycles from an initial rate of 5.94 $mL.min^{-1}$ in the first cycle to 2.1 $mL.min^{-1}$ in the fifth cycle. When adjusted for catalyst weight this equals 150.06 $mL.min^{-1}$ g_{cat}^{-1}. Literature reports in [17] of 4 moles of H_2 per mole of $NaBH_4$ in 33 minutes with a similar surface textured cobalt foam lead to the conclusion that this experimental method is significantly inefficient. In [23], similar yield was reported in just 10 minutes for cobalt anchored on polycarbonate membrane, albeit differing experimental conditions. The plot of hydrogen volume evolution with time is shown in figure 4.19 below.

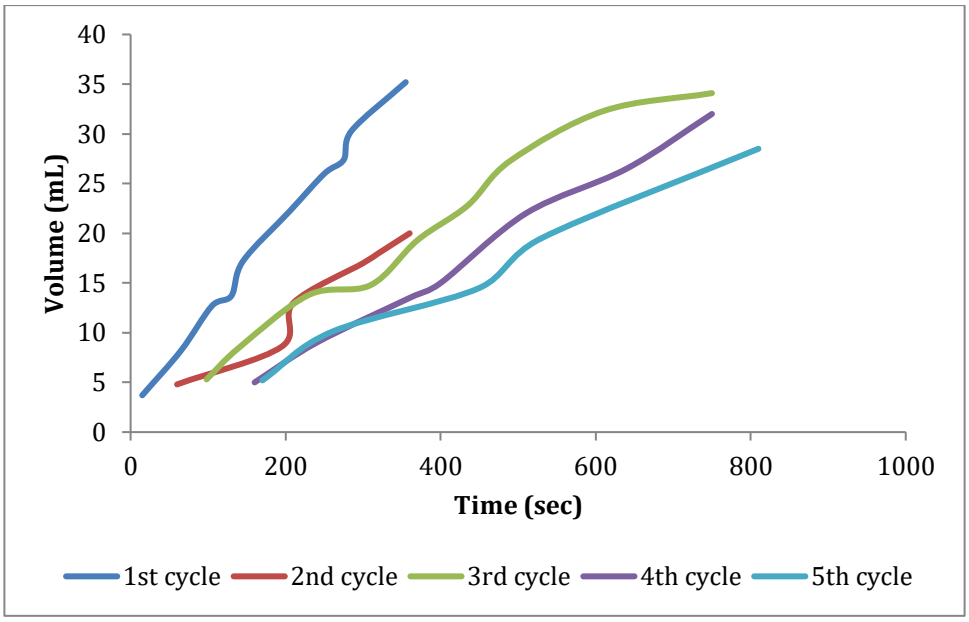

Figure 4.19: Sodium borohydride hydrolysis for Co_{100} foam using the inverted burette method.

Figure 4.20 below shows the hydrogen volume evolved performing the experiment in a milli gas counter.

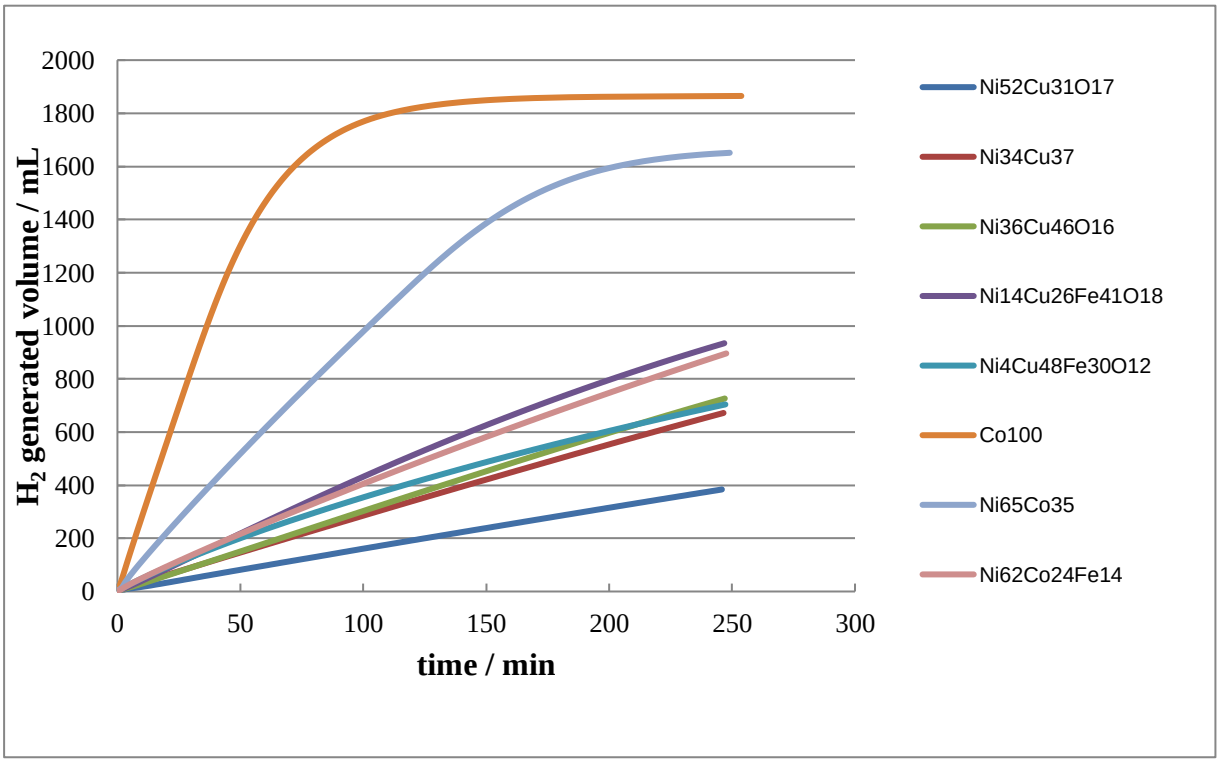

Figure 4.20: Hydrogen evolution curves for each foam in 5 wt.% $NaBH_4$ and 0.4 wt.% NaOH at 60 ˚C using the MilliGasCounter(Ritter).

Cobalt and its derivative foams were superior in performance towards hydrolysis of sodium borohydride, which explains the inferior performance to nickel based foams in the competing oxidation

reaction of borohydride. A maximum hydrogen evolution rate up to 30 mL.min^{-1} is obtained for pure cobalt foam.

The rate of evolution as shown in figure 4.21 below rises to a maximum, then becomes uniform for a short period before falling rapidly as the reaction approaches completion.

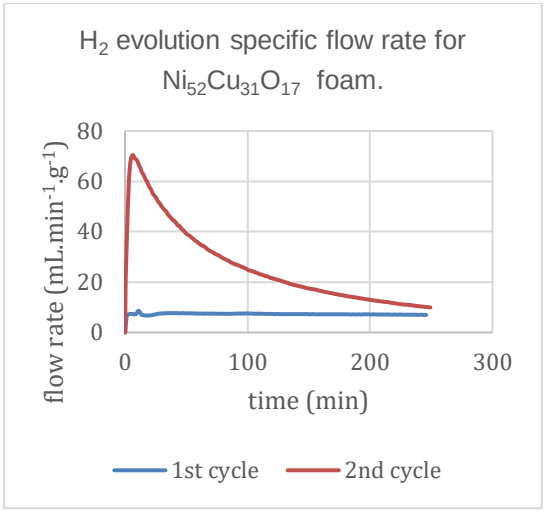

(a)

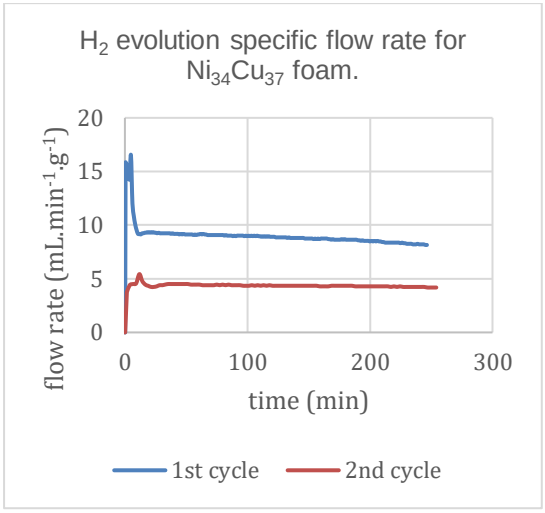

(b)

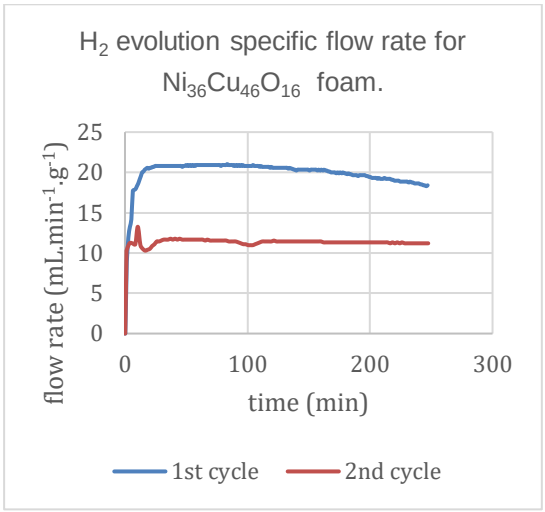

(c)

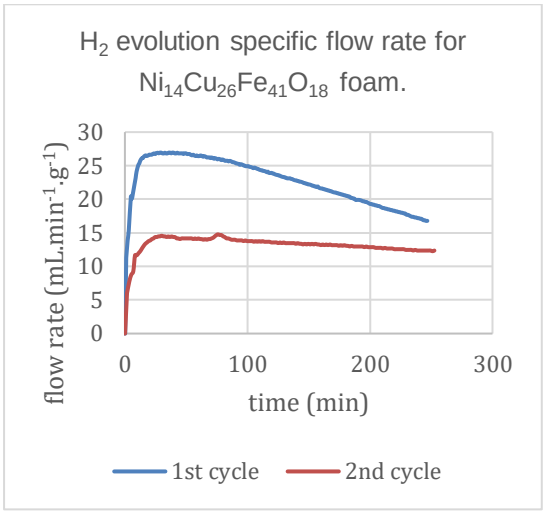

(d)

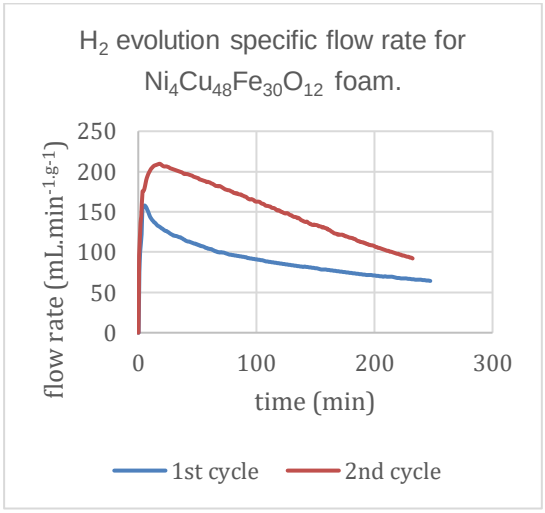

(e)

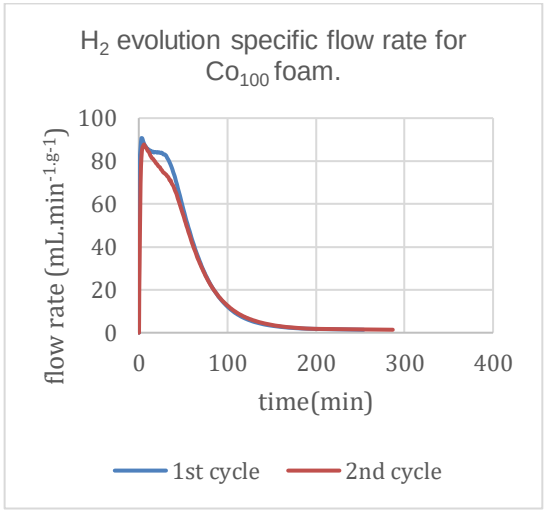

(f)

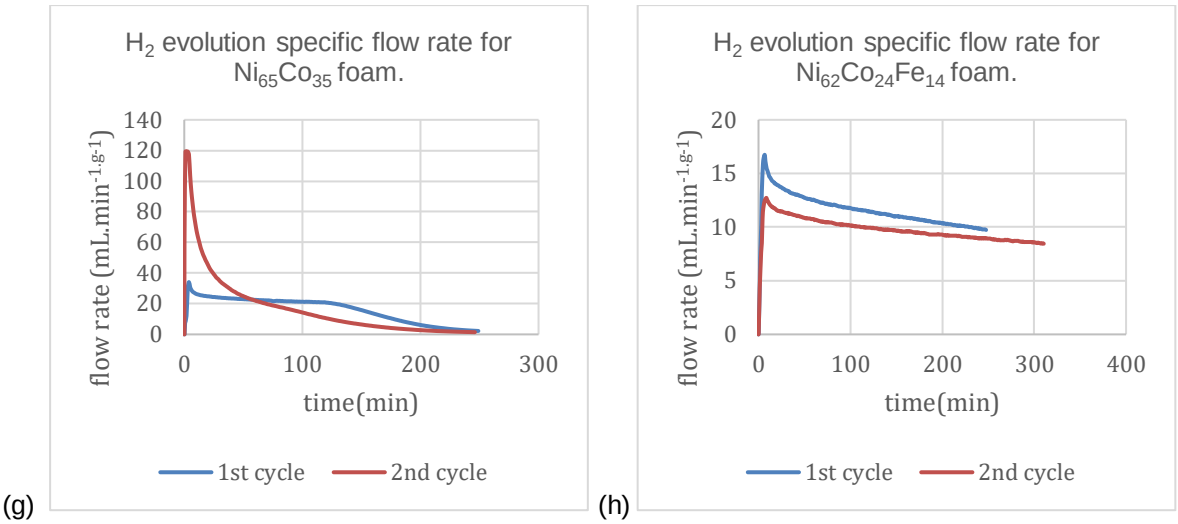

Figure 4.21: Flow rate per unit gram for the foams over two cycles in 5 wt.% $NaBH_4$ and 0.4 wt.% NaOH at 60 ˚C.

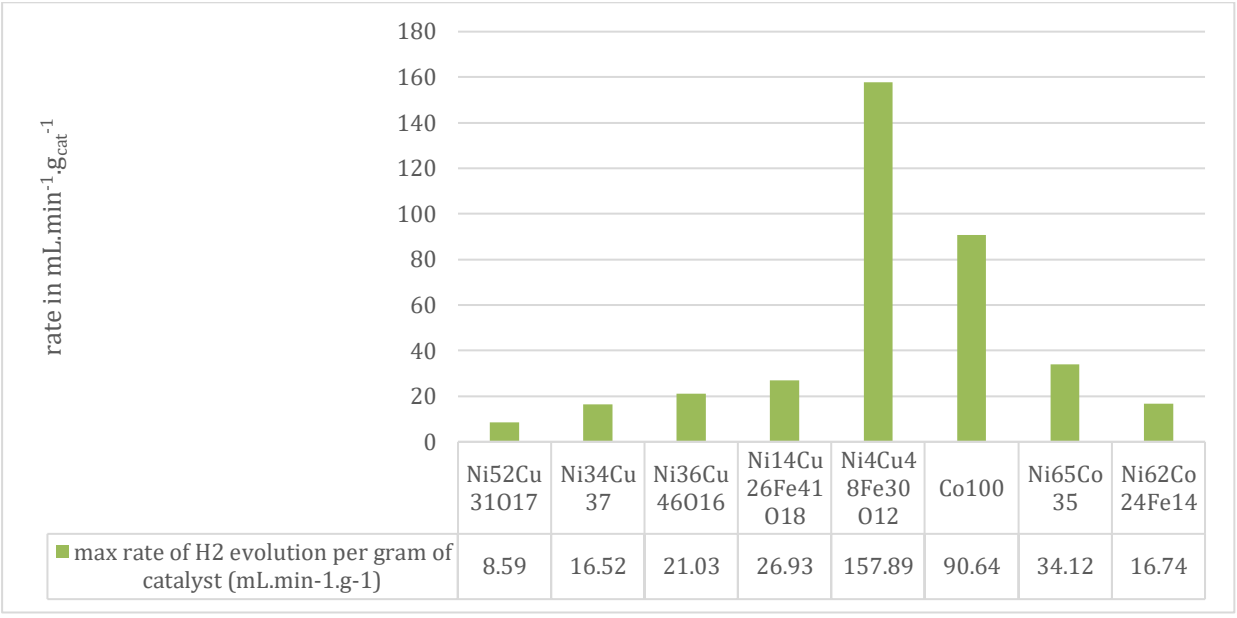

Figure 4.22: Maximum rate of H_2 evolution per gram of catalyst ($mL.min^{-1}.g^{-1}$).

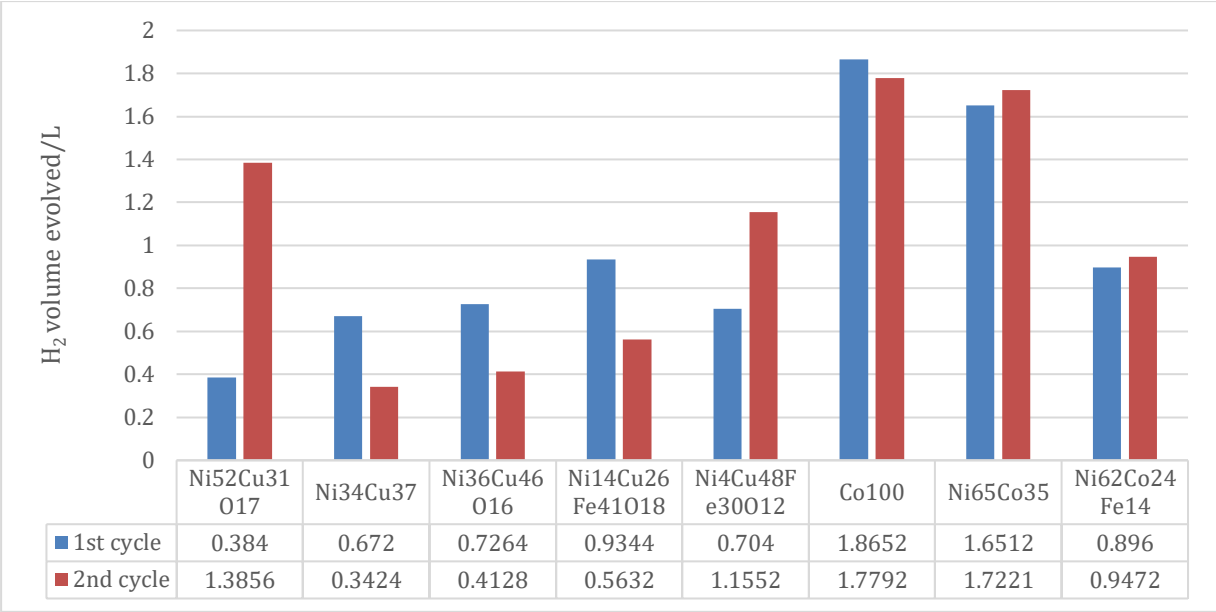

	Ni52Cu31O17	Ni34Cu37	Ni36Cu46O16	Ni14Cu26Fe41O18	Ni4Cu48Fe30O12	Co100	Ni65Co35	Ni62Co24Fe14
1st cycle	0.384	0.672	0.7264	0.9344	0.704	1.8652	1.6512	0.896
2nd cycle	1.3856	0.3424	0.4128	0.5632	1.1552	1.7792	1.7221	0.9472

Figure 4.23: Activity of foams through two cycles in 5 wt.% $NaBH_4$ and 0.4 wt.% NaOH at 60 ˚C.

We would expect loss of activity in the foams through successive cycles as pore spaces and active sites get blocked, however, as shown in figure 4.22 above, a few foams behaved in contrary. Intermediate oxides which improve the catalytic properties of the foams, formed on the surface of the catalysts, is the most plausible reason for this anomaly.

5 CONCLUSIONS

Co-deposition with the hydrogen bubble template presents an easy and efficient method to produce nanoporous three-dimensional metallic foams; whose synergistic performances can be optimized towards the exploitation of sodium borohydride properties either as a fuel in direct borohydride fuel cells or as a hydrogen carrier in indirect ones.

In terms of foam morphology, the following traits as observed are pivotal to catalyst design; nickel is largely credited for enhancing foam porosity with dendritic pore walls, copper is instrumental to obtain larger apparent pore sizes, iron improved the interconnectivity of the pores, while cobalt favors a 2D architecture-effectively reducing porosity with a characteristic shallowness of surface pores and a densely packed pore wall.

The ternary Ni-Cu-Fe foams presented the best performances towards sodium borohydride oxidation in terms of the current density per unit gram of catalyst, despite a low number of electron transferred in comparison with the binary Ni-Cu foam. Although cobalt foam and its derivative foams had been established as favoring the hydrolysis experiment, the ternary Ni-Cu-Fe foam, outperformed them in terms of rate per unit catalyst weight in the hydrolysis experiment as well.

Cobalt based foams produce hydrogen faster, however, the ternary $Ni_4Cu_{48}Fe_{30}O_{12}$ foams performs better when normalized for mass of catalyst.

6 FUTURE WORK RECOMMENDATIONS

- Alternative electrochemical analysis, such as rotating disc electrode using Koutecky-Levich equation can be used to confirm performance of the catalysts.
- The synergistic performance of ternary foams could be optimized.
- Other configurations of transition metals towards sodium borohydride fuel cells could be investigated.
- To examine improvements in number of electrons transferred, noble metals can be introduced by other electrodeposition methods like galvanic displacement.
- The effect of alternative electrodeposition techniques on morphology for similar foam compositions can be investigated.
- Characterization of catalytic foams after every reaction step can be used to verify the reaction mechanism, and provide insights on some of the observed anomalies.

7 BIBLIOGRAPHY

[1] A. K. Shukla, C. L. Jackson, and K. Scott, “The promise of fuel cell-based automobiles,” *Bull. Mater. Sci.*, vol. 26, no. 2, pp. 207–214, 2003.

[2] J. Larminie and A. Dicks, “Fuel Cell Systems Explained,” *2nd Ed. John Wiley Sons Ltd*, vol. 93, no. 1–2, pp. 14–16, 67–72, 2003.

[3] J. Ma, N. A. Choudhury, and Y. Sahai, “A comprehensive review of direct borohydride fuel cells,” *Renewable and Sustainable Energy Reviews*, vol. 14, no. 1. pp. 183–199, 2010.

[4] S. C. Amendola, P. Onnerud, M. T. Kelly, P. J. Petillo, S. L. Sharp-Goldman, and M. Binder, “A novel high power density borohydride-air cell,” *J. Power Sources*, vol. 84, no. 1, pp. 130–133, 1999.

[5] Z. P. Li, B. H. Liu, K. Arai, K. Asaba, and S. Suda, “Evaluation of alkaline borohydride solutions as the fuel for fuel cell,” *J. Power Sources*, vol. 126, no. 1–2, pp. 28–33, 2004.

[6] E. Gyenge, “Electrooxidation of borohydride on platinum and gold electrodes: Implications for direct borohydride fuel cells,” *Electrochim. Acta*, vol. 49, no. 6, pp. 965–978, 2004.

[7] S. Srinivasan, *Fuel Cells: From Fundamentals to Applications*, vol. 9, no. 10. McGraw Hill Publishing Company New York, NY., 2006.

[8] M. Chatenet, F. Micoud, I. Roche, and E. Chainet, “Kinetics of sodium borohydride direct oxidation and oxygen reduction in sodium hydroxide electrolyte. Part I. BH4\n- electro-oxidation on Au and Ag catalysts,” *Electrochim. Acta*, vol. 51, no. 25, pp. 5459–5467, 2006.

[9] M. H. Atwan, C. L. B. Macdonald, D. O. Northwood, and E. L. Gyenge, “Colloidal Au and Au-alloy catalysts for direct borohydride fuel cells: Electrocatalysis and fuel cell performance,” *J. Power Sources*, vol. 158, no. 1, pp. 36–44, 2006.

[10] B. H. Liu, Z. P. Li, and S. Suda, “A study on performance stability of the passive direct borohydride fuel cell,” *J. Power Sources*, vol. 185, no. 2, pp. 1257–1261, 2008.

[11] D. M. F. Santos, S. Eugénio, D. S. P. Cardoso, B. Šljukić, and M. F. Montemor, “Three-dimensional nanostructured Ni–Cu foams for borohydride oxidation,” *Russ. J. Phys. Chem. A*, vol. 89, no. 13, pp. 2449–2454, 2015.

[12] A. J. Bard and L. R. Faulkner, *Electrochemical methods: fundamentals and applications*, 2nd ed. John Wiley & Sons, Inc., 2001.

[13] “No Title.” [Online]. Available: https://www.chem.uci.edu/~ardo/echem/UCI-CHEM248-2017W_lecture14.pdf. [Accessed: 20-Aug-2017].

[14] B. J. Plowman, L. A. Jones, and S. K. Bhargava, “Building with bubbles: the formation of high surface area honeycomb-like films via hydrogen bubble templated electrodeposition,” *Chem. Commun.*, vol. 51, no. 21, pp. 4331–4346, 2015.

[15] Y. Wang, Y. Shen, K. Qi, Z. Cao, K. Zhang, and S. Wu, “Nanostructured cobalt-phosphorous catalysts for hydrogen generation from hydrolysis of sodium borohydride solution,” *Renew. Energy*, vol. 89, pp. 285–294, 2016.

[16] B. H. Liu, Z. P. Li, and S. Suda, “Nickel- and cobalt-based catalysts for hydrogen generation by hydrolysis of borohydride,” *J. Alloys Compd.*, vol. 415, no. 1–2, pp. 288–293, 2006.

[17] S. Eugénio, U. B. Demirci, T. M. Silva, M. J. Carmezim, and M. F. Montemor, “Copper-cobalt

foams as active and stable catalysts for hydrogen release by hydrolysis of sodium borohydride," *Int. J. Hydrogen Energy*, vol. 41, no. 20, pp. 8438–8448, 2016.

[18] Y. Wei, W. Meng, Y. Wang, Y. Gao, K. Qi, and K. Zhang, "Fast hydrogen generation from NaBH4 hydrolysis catalyzed by nanostructured Co–Ni–B catalysts," *Int. J. Hydrogen Energy*, vol. 42, no. 9, pp. 6072–6079, 2017.

[19] S. Eugénio, T. M. Silva, M. J. Carmezim, R. G. Duarte, and M. F. Montemor, "Electrodeposition and characterization of nickel--copper metallic foams for application as electrodes for supercapacitors," *J. Appl. Electrochem.*, vol. 44, no. 4, pp. 455–465, Apr. 2014.

[20] L. Vázquez-Gómez, E. Verlato, S. Cattarin, N. Comisso, P. Guerriero, and M. Musiani, "Electrodeposition of porous Co layers and their conversion to electrocatalysts for methanol oxidation by spontaneous deposition of Pd," *Electrochim. Acta*, vol. 56, no. 5, pp. 2237–2245, 2011.

[21] Santos, D. M F, Šljukić, B., Amaral, L., Milikić, J., Sequeira, C. A C, Macciò, D., Saccone, A. "Nickel-rare earth electrodes for sodium borohydride electrooxidation," *Electrochim. Acta*, vol. 190, pp. 1050–1056, 2016.

[22] B. H. Liu, Z. P. Li, and S. Suda, "Electrocatalysts for the anodic oxidation of borohydrides," *Electrochim. Acta*, vol. 49, no. 19, pp. 3097–3105, 2004.

[23] O. Akdim, R. Chamoun, U. B. Demirci, Y. Zaatar, A. Khoury, and P. Miele, "Anchored cobalt film as stable supported catalyst for hydrolysis of sodium borohydride for chemical hydrogen storage," *Int. J. Hydrogen Energy*, vol. 36, no. 22, pp. 14527–14533, 2011.